



Estimating near-shore wind resources

Floors, Rogier Ralph; Hahmann, Andrea N.; Peña, Alfredo; Karagali, Ioanna

Publication date:
2016

[Link back to DTU Orbit](#)

Citation (APA):

Floors, R. R., Hahmann, A. N., Peña, A., & Karagali, I. (2016). *Estimating near-shore wind resources*. DTU Wind Energy. DTU Wind Energy E No. 0116

General rights

Copyright and moral rights for the publications made accessible in the public portal are retained by the authors and/or other copyright owners and it is a condition of accessing publications that users recognise and abide by the legal requirements associated with these rights.

- Users may download and print one copy of any publication from the public portal for the purpose of private study or research.
- You may not further distribute the material or use it for any profit-making activity or commercial gain
- You may freely distribute the URL identifying the publication in the public portal

If you believe that this document breaches copyright please contact us providing details, and we will remove access to the work immediately and investigate your claim.

Estimating near-shore wind resources

DTU Wind Energy
E-Report

Rogier Floors, Andrea Hahmann, Alfredo Peña
and Ioanna Karagali

DTU Wind Energy-E-Report-0116 (EN)
Oktober 2016

DTU Wind Energy
Department of Wind Energy



Author: Rogier Floors, Andrea N. Hahmann, Alfredo Peña and Ioanna Karagali
Title: Estimating near-shore wind resources
Department: DTU Wind Energy

DTU Wind Energy
Report E-0116
October 25, 2016

Abstract (max. 2000 char)

An evaluation and sensitivity study using the WRF mesoscale model to estimate the wind in a coastal area is performed using a unique data set consisting of scanning, profiling and floating lidars. The ability of the WRF model to represent the wind speed was evaluated by running the model for a four month period in twelve different set-ups. The atmospheric boundary layer was parametrized using the first-order YSU scheme and the 1.5-order MYJ scheme. Simulations with two sources of land use data, two sources of reanalysis data, two sources of sea-surface temperatures and three different horizontal grid spacings were performed for each of the two schemes.

An evaluation of the wind profile using vertical profilers revealed small differences in modelled mean wind speed between the different set-ups, with the YSU scheme predicting slightly higher mean wind speeds. Larger differences between the different simulations were observed when comparing the root-mean-square error (RMSE) between modelled and measured wind, with the ERA interim-based simulations having the lowest errors. The simulations with finer horizontal grid spacing had a larger RMSE.

Horizontal transects of mean wind speed across the coastline measured with the scanning lidars were compared with the model simulations, showing that the shape of the horizontal gradient was well captured but the modelled mean wind speed was slightly overestimated. An evaluation of model performance with Taylor diagrams, showed that the sensitivity was largest to the PBL scheme and the reanalysis data. The simulations using the MYJ scheme had a lower RMSE and higher correlation coefficient than those using the YSU scheme, but also a lower variance compared to the observations. Using ERA interim instead of FNL as boundary conditions also led to a lower RMSE and correlation coefficient. Using a finer grid spacing of 1 and 0.5 km did not give better results and sensitivity to the input of different SST and land cover data in the RUNE area was small.

The difference in mean wind speed between all simulations over a region 80 km around the RUNE area were less than 1 m s^{-1} , with the largest differences over land due to the roughness length deviations and over sea due to SST differences. Simulations using the YSU scheme were more sensitive to variations in land use near the coastline, SST and forcing than those using the MYJ scheme. The forcing data had an impact on the simulated mean wind speed offshore, but the impact was negligible in the immediate RUNE region. The variance varied little as a function of the model grid spacing. Finally a wind resource estimation was made using the WAsP model, the mesoscale model and scanning lidar measurements and the uncertainties in each of the estimations is discussed.

ISSN:
ISBN:
978-87-93278-73-8

Sponsorship: The ForskEL programme, project nr. 12263 "RUNE"

Pages: 49
Tables: 7
Figures: 37
References: 29

Technical University of Denmark
Frederiksborgvej 399
4000 Roskilde
Denmark
Tel. +4546775024
roff@dtu.dk
www.vindenergi.dk

Contents

	Page
1 Introduction	5
2 Summary of measurement campaign	7
2.1 Vertical profiling lidar and meteorological masts	7
2.2 Cross sections	8
3 Mesoscale modeling	10
3.1 Basic setup	10
3.2 Special considerations for RUNE	11
3.2.1 PBL scheme	11
3.2.2 Horizontal grid spacing	11
3.2.3 Terrain elevation and land use	12
3.2.4 Sea surface temperature	13
3.2.5 Driving global analysis	13
4 Microscale modeling	13
5 Verification	15
5.1 Vertical profiles	15
5.2 Cross sections	19
5.3 Overall model performance	22
6 Analysis of mean wind speed during the full period	25
6.1 Effect of land, atmosphere and sea inputs	25
6.2 The effect of resolution	29
6.3 Examining the coastal gradient	34
6.4 Satellite-derived maps	39
7 Offshore wind resource estimation	41
8 Summary and recommendations	45
References	47
Appendix A CORINE roughness classification	49

1 Introduction

Many countries are investing in renewable energy sources such as wind energy. There is a strong interest to install near-shore wind farms, because of the high offshore wind speeds and relatively cheap grid connectivity. For estimating the wind resource, the Wind Atlas and Application Program (WAsP) and the Weather Research and Forecasting (WRF) model are often used. However, in the coastal area these models are often more uncertain, because of complex flow phenomena such as internal boundary layers (Floors et al., 2011), changing stability (Barthelmie, 1999), coastal low-level jets (Nunalee and Basu, 2014) and wave-atmosphere interactions (Lange et al., 2004). To assess and reduce the uncertainty in the estimation of offshore annual energy production, the output of these models has to be evaluated and their accuracy has to be improved.

The WRF model is frequently used for wind resource estimations (Guo et al., 2014; Badger et al., 2015; Sanz Rodrigo et al., 2016). Hahmann et al. (2015) used the WRF model to estimate the wind speed at 11 offshore and coastal sites and found that the differences between different set-ups in mean wind speed were relatively small. However, errors in the estimated wind speed were much higher at coastal than at offshore sites. Furthermore it was found that the variance in the WRF model was generally lower than observed. Floors et al. (2013) ran the WRF model with two different PBL schemes at a coastal site and found a large under estimation for both schemes in the modelled mean wind speed. Changing the atmospheric boundary conditions did not reduce this bias and the surface roughness description had impact on the wind speed near the ground.

Errors in wind speed predictions near the ground over land can often be related to misrepresenting the surface roughness length (Hahmann et al., 2015). The surface roughness is usually determined from satellite-based products of land cover, which are then converted to a look-up table with an approximate roughness length. This process thus relies on accurate representation of the land use. It was found that WRF-simulated 10-m winds and precipitation were closer to the observations in a set-up using CORINE compared to USGS land cover data (De Meij and Vinuesa, 2014).

Another problem with mesoscale modelling in the coastal zone is the limited horizontal grid spacing that can be used. With the current computational resources it is possible to perform mesoscale simulations with horizontal grid spacing from several kilometers down to several hundreds of meters. The latter configurations enter the domain of scales where turbulence has to be resolved, the ‘terra-incognita’ or grey zone (Wyngaard, 2004). At horizontal resolutions of ~ 100 m the mesoscale model also starts to resolve the growth of the internal boundary that develops after the change in surface roughness at the coastline. It can therefore be hypothesized that increasing the horizontal grid spacing can better represent a horizontal gradient in wind speed near the coast.

The sea-surface temperature (SST) can have a marked influence on the representation of the wind because it largely determines the offshore stability (Barthelmie, 1999). It is hypothesized that a high-resolution product is required to resolve well the stronger gradients in SST near the coast. Therefore we here use a new, high-resolution description of the SST in the North Sea and Baltic area (Høyer and Karagali, 2016).

The RUNE project used a single and dual scanning lidar setup, a lidar mounted on a buoy and vertically profiling lidars to measure the flow. The question of whether these instruments can accurately measure the wind speed in a coastal area is answered in detail in Floors et al. (2016a). In this report, we focus on the modelling of coastal flow by answering these research questions:

- Does the mesoscale model accurately represent vertical profiles and the coastal gradient of the mean wind speed?
- What is the sensitivity of mesoscale models to horizontal resolution, PBL scheme, atmospheric boundary conditions, land cover description and sea-surface temperature description and is there a preferred set-up?
- Can the measurements be used to improve the accuracy of a wind resource assessment?

To answer these questions we set-up 12 different versions of the WRF model. The simulations are performed with both the YSU (Noh et al., 2003) and the MYJ PBL scheme (Janjić, 1990). We use model set-ups with two SST descriptions, two land-cover descriptions and three different horizontal grid spacings. The simulations span the full four-month period during which measurements were available.

First we briefly summarize the different measurements to allow for their interpretation in Sect. 2. All details about the different mesoscale model setups are described in Sect. 3 and Sect. 4 details the WAsP model set-up. Sect. 5 reports on the evaluation of the model: both the vertical and the spatial profiles of mean wind speed are evaluated and we summarize overall model performance using Taylor diagrams. Sect. 6 then analyses the observed cross-sections and spatial maps of mean wind speed. Finally, in Sect. 7 we perform a wind resource assessment using the WAsP model with observed wind climates determined from different heights and locations and compare these with the WRF model and observations.

2 Summary of measurement campaign

We only briefly describe the measurements, because information about the campaign is described in more detail in Floors et al. (2016a). For convenience, the different lidars have been given names that will be used throughout this report (Table 1). The campaign was running from the beginning of November until February. In Table 1 the available measurements are shown and the corresponding position of each device is shown in Fig. 1. The scanning lidars Sterenn, Vara and Koshava were installed at the coastline to have an unobstructed field of view (Fig. 1).

All vertically profiling lidars were running in a Velocity Azimuth Display (VAD) mode. WLS66 and Alizé were positioned at the same location as Vara. 3E and Bura were positioned approximately 400 and 1000 m inland, respectively. The Høvsøre meteorological mast is located ≈ 6 km south and ≈ 2 km inland of Vara. Finally, a lidar buoy was operating at two different locations. It was located ≈ 8 km offshore until the 7th of December, when it was damaged by waves and lost its electricity supply. Due to the weather conditions it was not recovered before the 11th of February, after which it was measuring at position 7. Figure 7 in Floors et al. (2016a) contains all information about the availability of all instruments during the campaign.

The experimental area is generally covered with crop- and grasslands. South of Koshava there is dyke separating the beach from the inland area, whereas at the position of Vara and Sterenn there is a cliff at the coastline and terrain elevation is higher.

Pos.	Name	Type	Usage	Easting (m)	Northing (m)	Height amsl (m)
1	Koshava	WLS200S-007	Dual setup	446080.03	6259660.30	12.36
2	Vara	WLS200S-012	Sector scan	445915.64	6261837.49	26.38
2	Alizé	WLS70-001	Vertical Profile	445915.64	6261837.49	26.38
2	WLS66	WLS7-066	Vertical Profile	445915.64	6261837.49	26.38
3	Sterenn	WLS200S-006	Dual setup	445823.66	6263507.90	42.97
4	3E	WLS7-007	Vertical Profile	446379.30	6263251.46	43.18
5	Bura	WLS7-002	Vertical Profile	447040.74	6263273.41	24.93
6	Lidar Buoy Pos1	WLS7-277	Vertical Profile	438441	6262178	0.00
7	Lidar Buoy Pos2	WLS7-277	Vertical Profile	440616	6262085	0.00
8	Høvsøre mast	-	Mast	447642	6255431	0.32

Table 1. Positions, names, types, main scanning strategies (usage) and coordinates (UTM WGS84, Zone 32V) of the lidars during the RUNE campaign (see details in the text), including the information of the Høvsøre meteorological mast. The lidar buoy was used at two positions. The type is the commercial name given by the lidar manufacturer Leosphere

2.1 Vertical profiling lidar and meteorological masts

To show the availability of the measurements in the period that has been modelled, we compute a data recovery rate (Table 2). The period between the 2nd of November 2015 until the 1st of March 2016 (17281 10-minute mean wind speeds) is available from the model simulations and is taken as 100%.

The meteorological mast at Høvsøre had a data recovery rate of nearly 95% and therefore represents well the true distribution of wind speeds during the modelling period. The vertical profiling lidars had a lower recovery percentage because they started measuring a few days after the beginning of the model simulations and because of filtering. All measurements up to 130 m had to have a CNR lower than -22 dB. These limits are the same as described in Floors et al. (2016a), where extensive comparisons between the different measuring systems can also be found. The CNR criterion for Alizé was reduced to -32 dB because we performed a com-

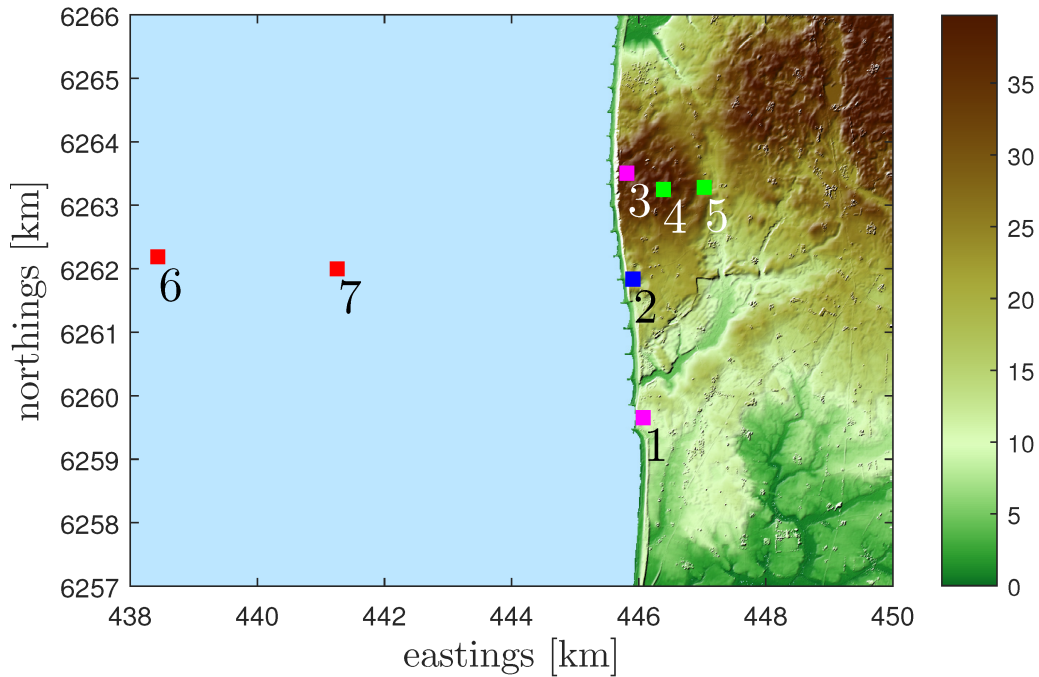


Figure 1. Topographic description (colours) of the terrain around the experimental site and the positions of the lidars denoted with numbered points (Table 1). The vertically profiling lidars WLS66 and Alizé are collocated with Vara in position 2.

parison up to 500 m height and the amount of data was significantly reduced when using higher CNR limits. For the lidar buoy the recovery percentage is much lower, due to the long period of unavailability described in the previous section.

Name	Loc.	N	Recovery [%]	Heights [m]
Høvsøre Mast	8	16383	94.80	10,40,60,80,100,160
Alizé	2	9866	57.09	100,150,175,200,250,300,350,400,450,500
Bura	5	10910	63.13	50,62,75,87,100,112,125
WLS66	2	9866	57.09	40,50,60,74,80,90,100,110,124
3E	4	13580	78.58	40,57,70,88,107,125
Lidar buoy	6	3859	22.33	43,50,62,82,100,120,137,150,175,200,212,250
Lidar buoy	7	1375	7.96	43,50,62,82,100,120,137,150,175,200,212,250

Table 2. Summary of the availability after filtering of the measurements at different locations. The number of observations is denoted with N .

2.2 Cross sections

To spatially evaluate the wind fields of the model setups, we will use the transects available from the scanning lidars during phase 2 and 3, i.e. from the 26th of November until the 17th of February. In this period Koshava and Sterenn were performing a scanning pattern at 50, 100 and 150 m height in a transect across the coast (Fig. 2). The most westward and eastward position were at ≈ 5 km offshore and 4 km inland, respectively. During the same period, Vara was performing a sector scan up to a maximum range of 8 km offshore. The availability of the scanning lidars is lower than from the lidars in VAD mode, because of the long distance to the the sampling point. Similarly to the profiling lidars we require measurements in all range gates to fulfill a CNR

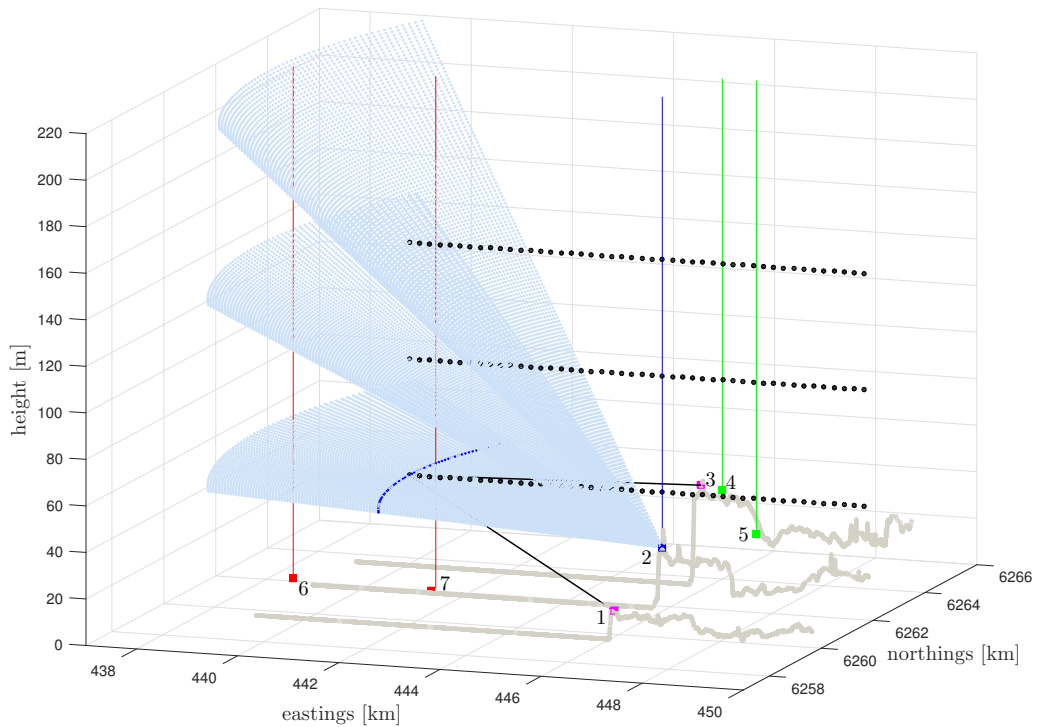


Figure 2. Overview of the scanning patterns during phase 2 and 3 of the RUNE campaign. The light blue points denote the sector scan from Vara, the black dots denote the collocated range gates from Sterenn and Koshava, the green lines denote the lidars 3E and Bura, the blue line denotes the lidars WLS66 and Alizé and the red line denotes the lidar buoy in it's second position. The dark blue points from the sector scan denote an arch from which the wind vector can be reconstructed.

threshold.

For the dual setup the CNR limit was -26.5 dB, whereas for the lidar in sector-scan mode the limit was -27 dB. Finally the measurements from the sector-scan and the dual setup are merged with the vertical profiling lidars. Because of the filtering the availability is reduced and the recovery percentage lower (Table 3). Therefore, we use a data set with a shorter range (2000 m west to 1500 m east of Vara) and a higher recovery percentage and one with a longer range (5000 m west to 2000 m east of Vara) but lower recovery percentage. Data more than 2000 m inland were not available due to the lidar beam hitting targets (Floors et al., 2016a).

Range [m]	N	Recovery [%]
-	17281	100.00
2000–1500	2605	15.07
5000–2000	832	4.81

Table 3. The availability of the cross sections in a specified range, by combining data from Alizé, WLS66, 3E, Bura and the dual setup and sector scans. The number of 10-min observations is denoted with N .

3 Mesoscale modeling

3.1 Basic setup

The Weather Research and Forecasting (WRF) model version 3.6 was used for simulating the wind conditions during the RUNE campaign (Skamarock et al., 2008). The development of this community model is led by the National Centre for Atmospheric Research (NCAR). Patches and bug fixes were applied to the model as described on <http://www2.mmm.ucar.edu/wrf/users/wrfv3.6/known-prob-3.6.html>. Using the WRF model version 3.6.1 and higher resulted in runtime errors when running in parallel on the high-performance computing cluster that is used at DTU Wind Energy. Because of the large number of simulations that had to be performed, it was chosen to use version 3.6 that was working well in parallel setup. A summary of the WRF model setup is provided in Table 4.

Model setup:
WRF (ARW) Version 3.6 with patches
Mother domain (D1; 1638 km × 1170 km); 2 nested domains: D2 (564 km × 564 km) and D3 (296 km × 296 km) on a Lambert Conformal projection (see Fig. 3).
70 vertical levels with model top at 50 hPa; The first 10 levels are located approximately at: 5.6, 17.4, 29.7, 42.7, 56.5, 71.0, 86.3, 102.5, 119.7 and 137.8 m.
Changes to lakes for better representation of inland water bodies.
Simulation setup:
Runs are started (cold start) at 12:00 UTC every day and are integrated for 36 hours, the first 12 hours of each simulation are disregarded.
Model output: 10-minutes (lowest 35 vertical levels) for D3 and D4, hourly for D1 and D2. Time step 65.455 seconds in D1.
One-way nested domains; 5 grid point nudging zone.
Spectral nudging on D1 only and above level 25; wavenumber 15 and 11 in the zonal and meridional direction. Nudging coefficient 0.0003 s^{-1} for wind, temperature and specific humidity. No nudging in the PBL.
Physical parameterizations:
Precipitation: WRF Single-Moment 5-class scheme (option 4), Kain-Fritsch cumulus parameterization (option 1) turned off on D3 and D4.
Radiation: RRTMG scheme for longwave (option 4); RRTMG scheme for shortwave (option 4)
Noah Land Surface Model (option 2).
Modified land use table where surface roughnesses are kept constant at their winter (lower) value.
Diffusion: Simple diffusion (option 1); 2D deformation (option 4); 6th order positive definite numerical diffusion (option 2); rates of 0.06, 0.08, and 0.1 for D1, D2, and D3, respectively; vertical damping.
Positive definite advection of moisture and scalars.

Table 4. Summary of model and system setup and physical parameterizations used in the simulations.

A set-up of three domains covering northern Europe was used, except for the simulations with the highest resolution which had 4 domains (Fig. 3). The extent of the outer domain is constrained by the availability of SST data described in Høyer and Karagali (2016). The boundaries of all domains were chosen such that they were at approximately the same location for the different

horizontal grid spacings.

The model was started every day at 00:00 UTC. Allowing a 12-h spin-up period, the model fields from 12 to 36 h were used to generate a continuous time series with a temporal resolution of 10 min. Pre-experiments were performed and showed that the RMSE between the wind speed of the model and observations at Høvsøre and Østerild was lowest when using a rather short simulation period of 24 hours.

The time step in the model was 65 s for the outermost domain and decreased with factors 3 and 9 in model domains 2 and 3, respectively. Seventy vertical model levels were used, which were densely spaced within the lower km of the atmosphere and a gradually decreased spacing at higher heights. The upper boundary of the domain was at 50 Pa.

Spectral nudging was used in the outermost domain above the 25th model level (≈ 600 m) and above the PBL. Spectral nudging is used because it gives a more realistic representation of the wind speed variance than grid nudging (Vincent et al., 2015). The maximum nudged wave numbers in the zonal and meridional direction were 15 and 11, respectively. The nudging coefficient was 0.0003 s^{-1} for wind, temperature and specific humidity.

3.2 Special considerations for RUNE

3.2.1 PBL scheme

In this report we use the YSU and MYJ PBL schemes, which are a first-order and 1.5-order closure scheme, respectively (Noh et al., 2003; Janjić, 1990). The simulations performed with a certain scheme are denoted in Table 5 with either YSU or MYJ. The abbreviations used in this table will be used throughout this report to denote different model simulations.

3.2.2 Horizontal grid spacing

The grid spacing ratio between the different nested domains is three. Three model set-ups with different horizontal grid spacing were used: the first two have a grid spacing of 2 and 1 km in the third (innermost) domain, whereas the third one has also a fourth domain with a grid spacing of 500 m. These three different runs are denoted with the subscript 2, 1 and 0.5. Furthermore we can extract output from the other domains to obtain grid spacings of 3, 4.5 and 6 km. The impact of different horizontal grid spacings on the land cover representation is shown in Fig. 4.

Model Simulation	Bound. cond.	PBL scheme	SST source	land-cover source	horizontal grid spacing [m]
YSU ₂	FNL	YSU	DMI	CORINE	2000
YSU ₁	FNL	YSU	DMI	CORINE	1000
YSU _{0.5}	FNL	YSU	DMI	CORINE	500
MYJ ₂	FNL	MYJ	DMI	CORINE	2000
MYJ ₁	FNL	MYJ	DMI	CORINE	1000
MYJ _{0.5}	FNL	MYJ	DMI	CORINE	500
YSU _{HRSSST}	FNL	YSU	HR	CORINE	2000
MYJ _{HRSSST}	FNL	MYJ	HR	CORINE	2000
YSU _{USGS}	FNL	YSU	DMI	USGS	2000
MYJ _{USGS}	FNL	MYJ	DMI	USGS	2000
YSU _{ERA}	ERA	YSU	DMI	CORINE	2000
MYJ _{ERA}	ERA	MYJ	DMI	CORINE	2000

Table 5. Abbreviated name, boundary conditions, PBL scheme, SST source, land-cover source and the horizontal resolution of the innermost domain of the modelling set-ups used during the RUNE campaign.

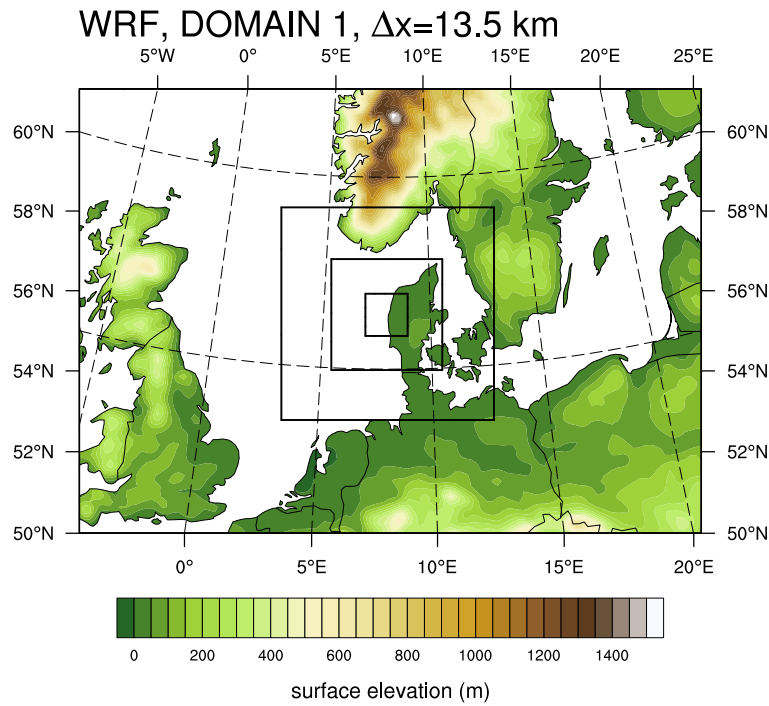


Figure 3. Surface elevation (m) of the outer domain with the location four nested model domains indicated.

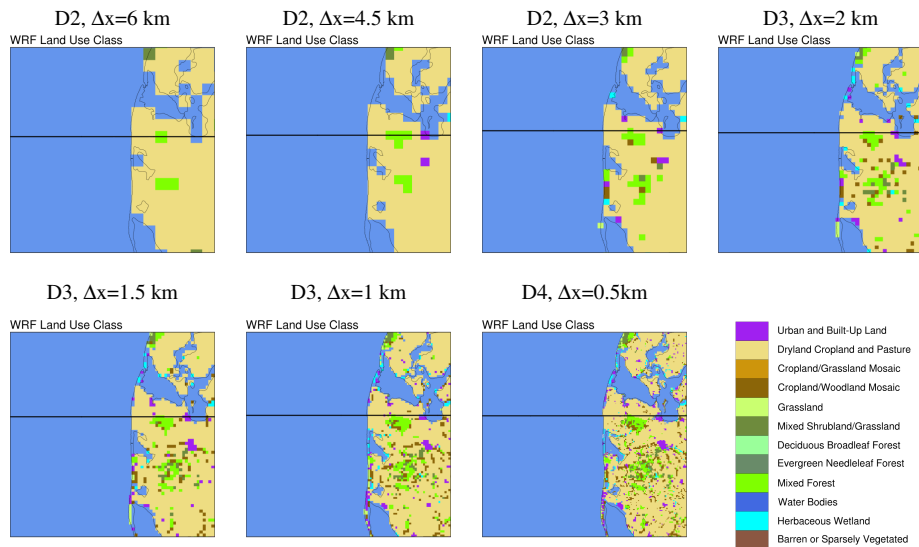


Figure 4. Land use classes derived from the CORINE dataset in the region of the fourth domain. The solid line shows the location of the cross section analyzed in Sec. 6.3.

3.2.3 Terrain elevation and land use

A spatial description is needed to set the physical properties of the surface, such as albedo, emissivity and the roughness length. The default land-use description that is provided with the WRF model is based on the 24-category land-use classes provided by the United States Geological Survey (USGS) (Anderson et al., 1976). In previous work it was found that the land use in Denmark is not very well captured in the data provided by the USGS (Nielsen, 2013). This is partly because the USGS data were gathered in 1992 and are outdated now due to changes in land cover.

Therefore, another source of land use data was used: the CORINE land cover data set was initiated in 1985 to provide an up-to-date description of land use in Europe and can be freely downloaded online (<http://www.eea.europa.eu/data-and-maps/data/CORINE-land-cover-2006-raster-3#tab-metadata>). Here we use the data created using satellite imagery from 2006. The 250 m product provides enough spatial resolution to represent the simulations with the highest horizontal resolution of 500 m (Table 5). The CORINE landuse data provides 44 landuse classes, but these were remapped to the same 24 landuse classes used in the USGS data (Pindea et al., 2002). This was done because roughness and moisture values cannot be obtained from the CORINE data and therefore have to be obtained from the USGS look-up table.

In addition to the 24 land use categories, one land use category is used for describing lakes. This is done because the water temperatures are otherwise set to the sea surface temperature. This can lead to large discrepancies in observed and modelled water temperatures, for example in winter when lakes are frozen in reality but are modelled using the high SST from the North Sea. Modified SRTM data with a horizontal grid spacing of 90 m was used (<http://www.viewfinderpanoramas.org/dem3.html>) for describing the terrain elevation in the WRF model.

3.2.4 Sea surface temperature

The National Centers of Environmental Prediction (NCEP) provide a real-time global (RTG) daily high-resolution (HR) daily SST analysis at a resolution of $1/12^\circ$ (Gemmill, W. and Katz, B. and Li, 2007). In Table 5 this SST product is abbreviated as HR. Because of the stronger SST gradients near the coast, we also used a new high-resolution product developed by the Danish Meteorological Institute (DMI). The Level 4 DMI North Sea-Baltic Sea daily analysis has a resolution of 0.02 degrees (Høyer and She, 2007). It has been specifically developed taking into consideration the conditions occurring in the Scandinavian region. With its temporal span from 1982 to now, it is appropriate for reproducing the climatic conditions (Høyer and Karagali, 2016). These data were provided by GHRSSST, DMI and the MyOcean regional data assembly centre.

3.2.5 Driving global analysis

The atmospheric boundary conditions were obtained from two sources: the Final Analysis (FNL) from the National Centre of Environmental Prediction (NCEP) and the ERA Interim Reanalysis (Saha et al., 2010; Dee et al., 2011). Because the ERA Interim data are not real time available, the RUNE simulations were mostly performed with the FNL data. The horizontal grid spacing of the FNL data is 0.25° , whereas it is about 0.78° for the ERA interim data.

4 Microscale modeling

The WAsP software is often used in wind resource estimations and will be used as a reference to horizontally and vertical extrapolate the wind speed. Version 11.4 is used here, available at <http://www.wasp.dk>. The software requires a map of the elevation and surface roughness length around the site. The 1.6-m resolution digital elevation model data from the Geostyrelsen in Denmark is used to describe the terrain height (<http://download.kortforsyningen.dk/content/dhm-2007overflade-16-m-grid>). The data is then resampled to a 15 m grid by averaging to avoid a too large file.

For the roughness estimation we use the CORINE data discussed in the previous section, but with a horizontal resolution of 100 m. The land-cover classes are then converted to roughness lengths corresponding to the values recommended in Troen and Petersen (1989) (Appendix A, Table 7). We use the model as recommended in Troen and Petersen (1989), including the default stability settings, -40 W m^{-2} over land and -8 W m^{-2} over sea. The root-mean-square of the heat flux parameter is set to 100 and 30 W m^{-2} over land and sea, respectively. However,

due to the limited period of measurements during the RUNE campaign, the observed stability is probably different from the default values which are more representative of the annual means.

5 Verification

5.1 Vertical profiles

The wind speed profile can show us how the different model set-ups describe the flow transition from sea to land. Figure 5 shows the wind speed from the set-ups using the MYJ PBL scheme at the locations given in Table 1. The number of samples at each of the locations is given in Table 2. The first panel shows the combined measurements of Alizé and WLS66 from 40 to 500 m at location 2, which is ≈ 100 m east of the coastline. It can be seen that all model set-ups give very similar mean wind speeds.

The observations show a slightly higher mean wind speed, mostly at higher heights. At the lowest measuring height the modelled wind speed is lower than the observed one, possibly due to the orographic effects from the cliff at this location. At locations 4 and 5, the wind speed near the ground is lower than at location 2 as expected from their positions inland. The higher surface roughness has slowed down the flow at these locations, which are approximately 1 and 2 km inland, respectively. Also at these locations, the effect of using different modelling setups on the mean wind speed is very small.

At the offshore locations of the lidar buoy, locations 6 and 7, it can be seen that there are larger differences between the different model set-ups. The set-up using the ERA interim as boundary conditions has the lowest mean wind speed and the set-up with 500 m horizontal grid spacing has the highest mean wind speed. At greater heights, all model set-ups under estimate the mean wind speed.

At the Høvsøre meteorological mast (Location 8) it can be seen that all model set-ups slightly over predict the mean wind speed, particularly at heights above 100 m. The differences in mean wind speed between the different model set-ups are very small at 500 m. Near the surface, the MYJ_{USGS} set-up overpredicts the mean wind speed. Fig. 6 showed the same variations of the model simulations as Fig. 5, but for the YSU PBL scheme. It can be seen that the variation of the mean wind speed with height is captured slightly better, resulting in a smaller difference between the mean wind speed from the simulations and observations at the highest available height for locations 2, 4, 6 and 7.

In Fig. 7 the mean wind speed bias between the MYJ model simulations and the observations is shown. At locations 2, 4, 6 and 7, which are close to the coast or offshore, the model simulations have a negative bias and under predict the wind speed. At location 2, close the coastline, the negative bias is largest near the ground and reduces higher up. At locations 5 and 8, which are more inland, the model simulations show a positive bias. For the YSU schemes, there is also a negative bias at locations 2, 4, 6 and 7, but it is smaller than that found when using the MYJ scheme. Particularly offshore the mean bias is very close to zero.

Although interesting from a wind resource perspective, the mean wind speed does not tell us how well the different set-ups predict the wind speed in each 10-min interval in the period; therefore the the root-mean-square error (RMSE) between the modelled and measured wind speed for each height and location was computed (Fig. 9). Using this metric, larger differences between the different set-ups are observed: the YSU₁ simulation shows the highest RMSE in most locations, followed by the YSU_{0,5} and YSU₂ simulations. The YSU_{ERA} simulations have the lowest RMSE, except for the offshore location 7, where the YSU_{HRSST} shows the lowest RMSE. This could indicate that for the offshore location HRSST describes the SST slightly better than the DMI SST in this area.

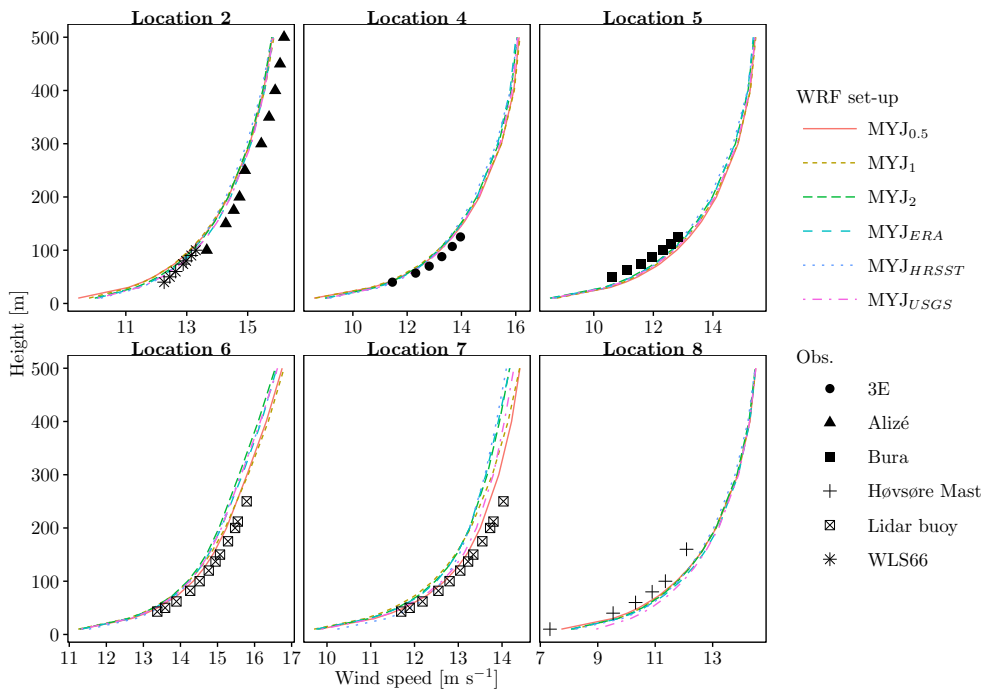


Figure 5. The mean wind speed between 10 and 500 m during the RUNE campaign using the simulations with the MYJ PBL scheme (Table 5) at different locations (Table 1). The number of available 10-min intervals for each panel is shown in Table 2.

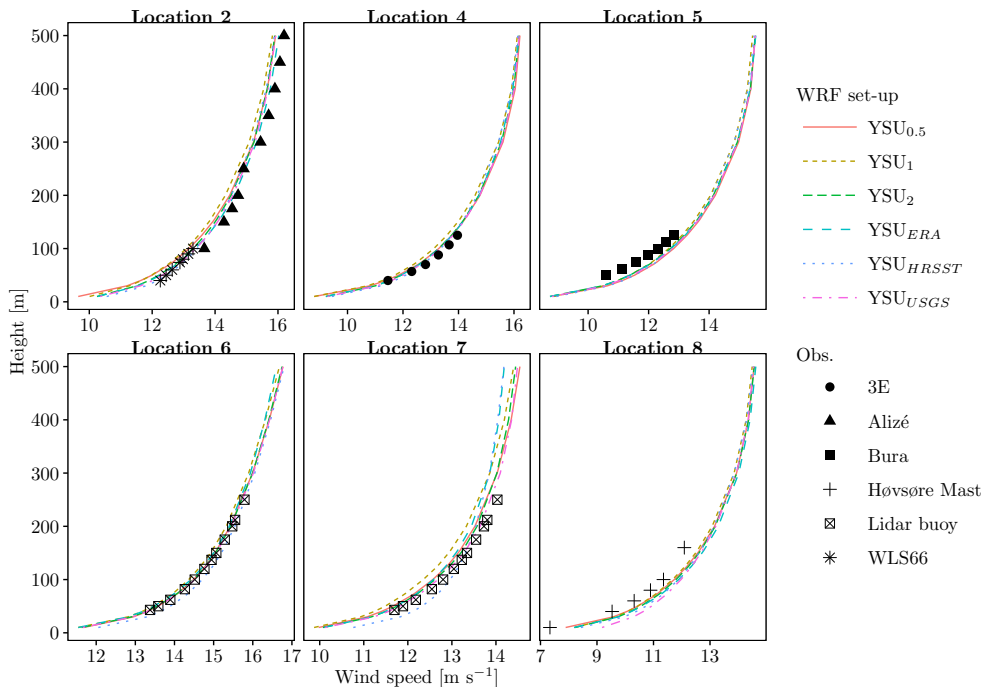


Figure 6. As Fig. 5, but using the YSU PBL scheme.

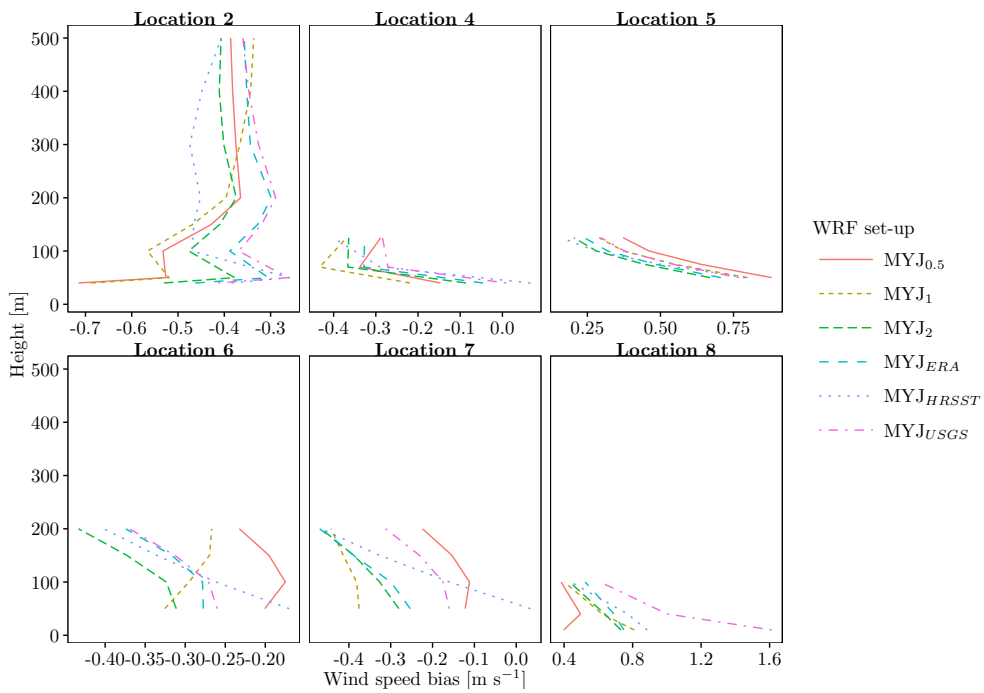


Figure 7. As Fig. 5, but showing the mean wind speed bias between the model set-ups and the observations.

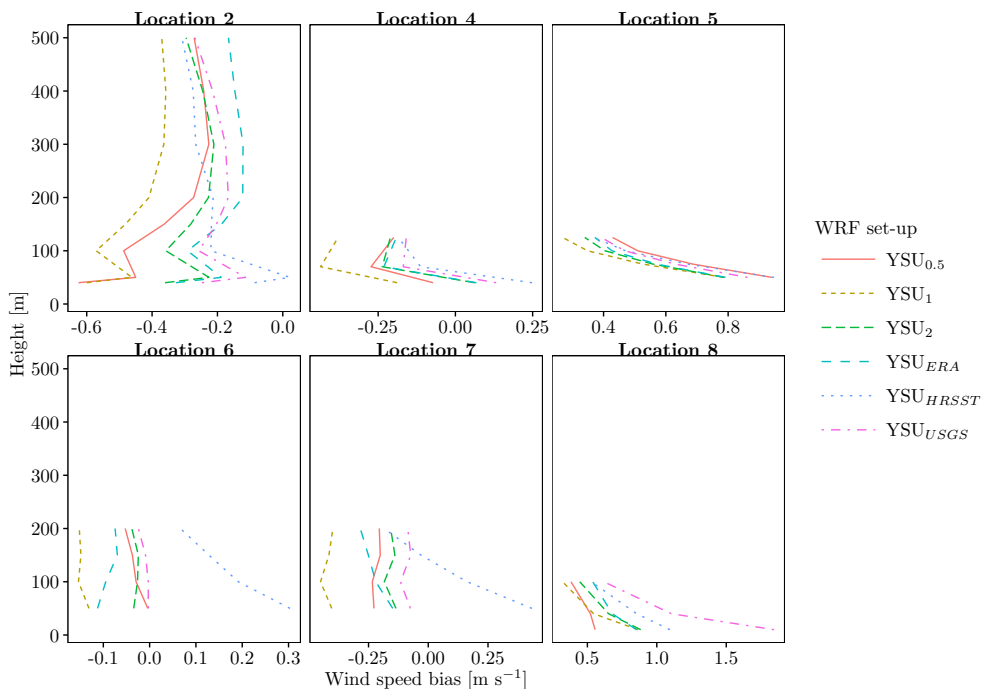


Figure 8. As Fig. 7, but using the YSU PBL scheme.

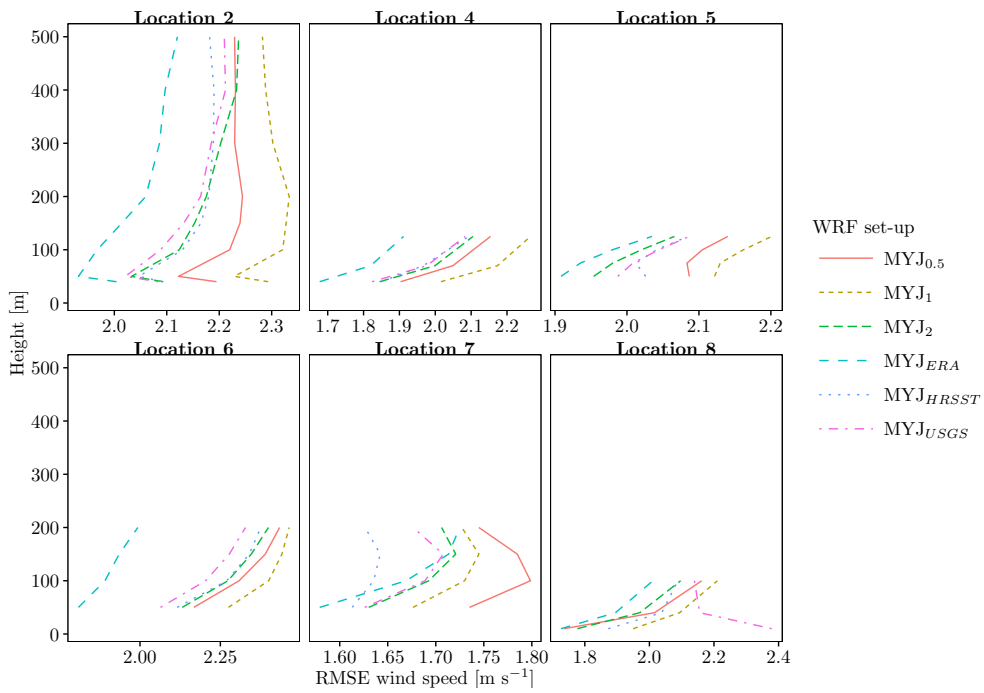


Figure 9. As Fig. 5, but showing the RMSE error between the modelled and the observed wind speed.

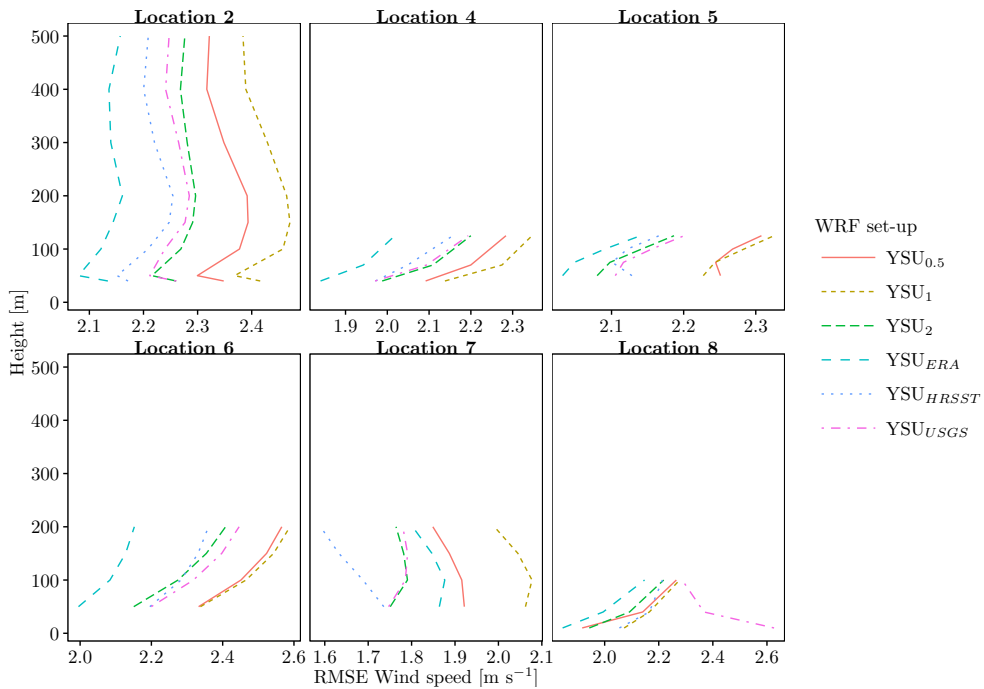


Figure 10. As Fig. 9, but using the YSU PBL scheme.

5.2 Cross sections

We use data from the dual and sector-scan setup and from the vertical profiling lidars 3E, Bura and WLS66 that fulfill the filtering criteria within a range of 5000 m offshore to 2000 m inland. The available 10-min intervals are then combined with the model output at these time steps and a mean wind speed at 50, 100 and 150 m is computed (Fig. 11).

It can be seen that the offshore mean wind speed is about 14 m s^{-1} at 50 m and decreases to about 11 m s^{-1} at 2 km inland (upper panel). There is a fairly good agreement in mean wind speed between the sector scan and dual setup, as further discussed in Floors et al. (2016a). Most model simulation agree within 0.5 m s^{-1} with the observations offshore, but inland all model simulations show higher wind speeds than observed.

At 100 m the wind speed from the model simulations show a slight over prediction of the mean wind speed both offshore and inland (middle panel). The vertical profiling lidars show lower wind speeds than the dual setup, which for 3E and Bura might be because they are measuring at a position North of the dual setup sampling point. The decrease in wind speed west of the coastline can be due to the uncertainty in the reconstructed wind speed when the two scanning lidar beams are facing each other and due to slow down of the flow because of the blocking effect of the cliff. The increase in mean wind speed east of the coastline can be due to reconstruction uncertainty or orographic speed-up. At 50 m the increase in wind speed is lower partly because the speed-up east of the coastline is compensated by a decrease in wind speed due to the decrease in measuring height; the sampling points offshore are at 50 m asl (above sea level) and inland they are about at 25 m agl.

At 150 m the mean wind speed offshore is about 15 m s^{-1} and is slightly higher for the model simulations compared to the observations (lower panel). The decrease of wind speed over land is much lower than at 50 m because the effect of the higher land roughness is smaller at this height.

Because the amount of transects that reach 5 km offshore is low, Fig. 12 shows the transects reaching up to 2 km only. This increases the percentage of the model simulations that is covered from 5 to 15% (Table 3). However, using this longer period does not have a significant effect on the qualitative findings based on Fig. 11: most model simulations over estimate the wind speed both offshore and onshore, although the difference is slightly smaller than in Fig. 11. An interesting feature is that the mean wind speed in Fig. 11 is much higher than in Fig. 12. This will be further discussed in Sect. 7.

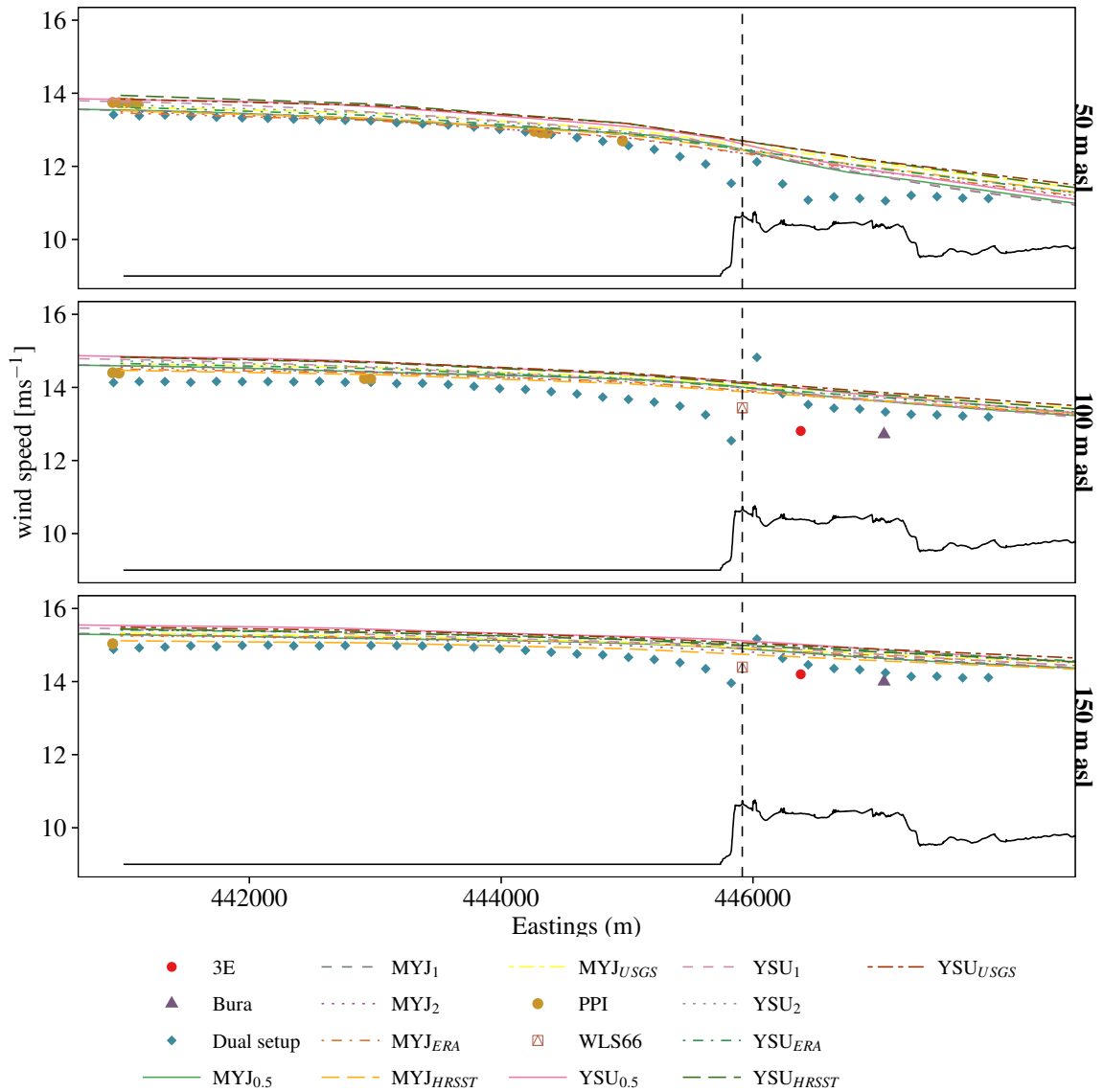


Figure 11. The reconstructed mean wind speed obtained from the sector-scan and dual setup and the vertical profiling lidars between 5000 m offshore and 2000 m inland (points) and the simulations (lines, Table 5). The number of available transects is shown in Table 3.

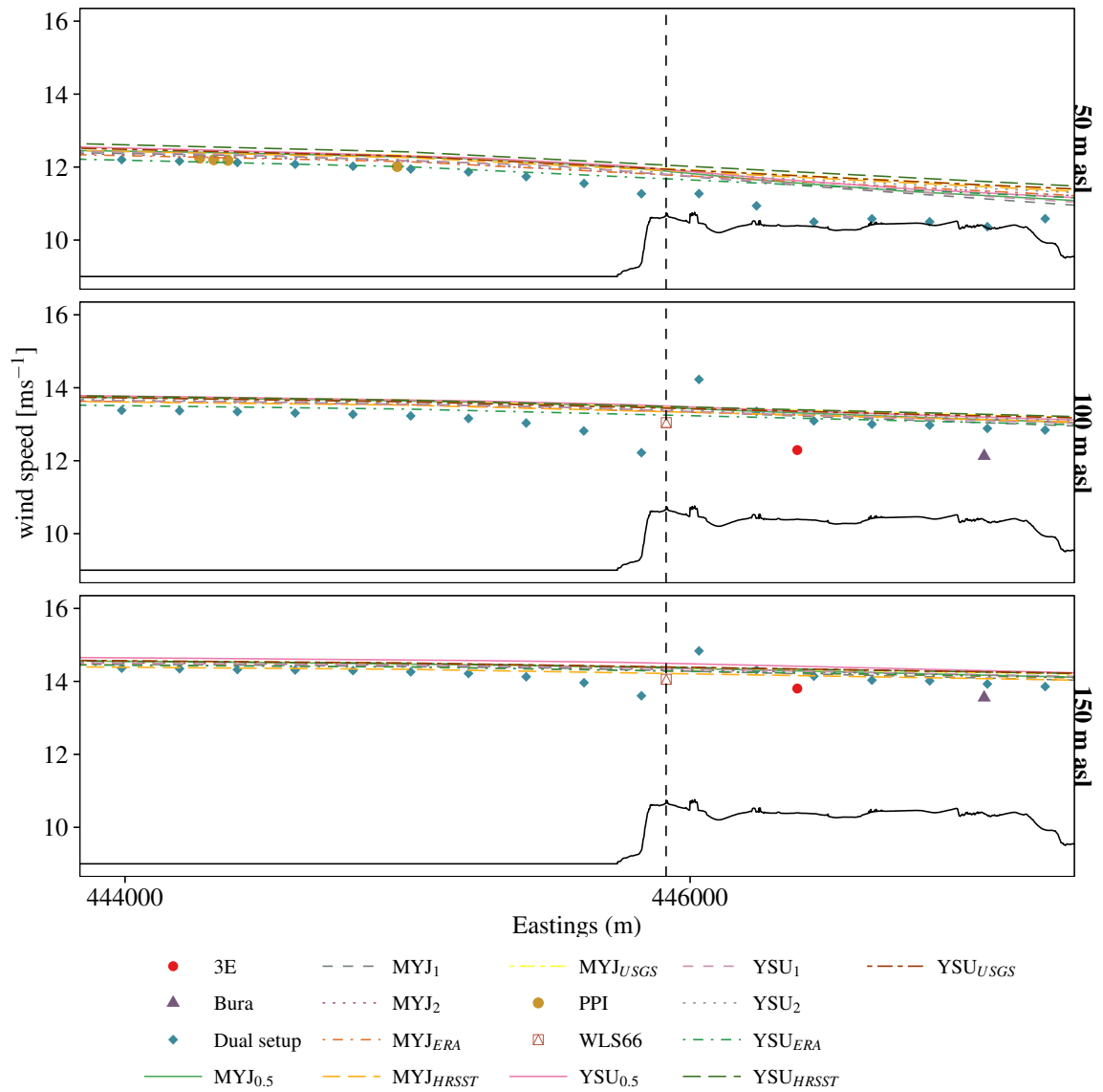


Figure 12. As Fig. 11, but using the data between 2000 m offshore up to 1500 m inland.

5.3 Overall model performance

For evaluating overall model performance we use Taylor-diagrams (Taylor, 2001). This is a diagram that combines the correlation coefficient, standard deviation and centred RMSE in one diagram and therefore gives a good overview of the model performance. The Taylor diagram with the different simulations is shown in Fig. 13 (left panel). The RMSE increases when the model results denoted by a point are further away from the observations (purple point), whereas the correlation coefficient decreases counterclockwise radially. The standard deviation is denoted by the distance from the origin. The closer the points from different simulations are to the observations, the better the model performance. Because the performance of the setups is rather similar, the right panel zooms in on the area denoted with a dotted line (left panel). This zoomed area is used for all Taylor-diagrams in this section. In the remainder of this section the scales are left out because we focus on the change in position of the point denoting the error metrics from different set-ups.

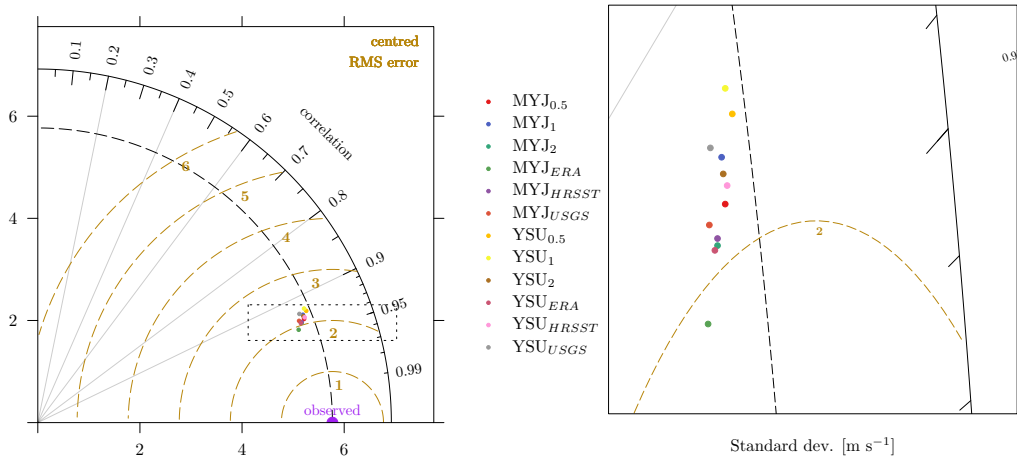


Figure 13. Taylor diagrams of overall model performance during the RUNE campaign using all 401974 10-minute intervals from all lidars in VAD mode and the meteorological mast at all available heights. The right panel provides a close-up of the left figure.

We first compare the simulations from Table 5 that are identical, except for changing the PBL scheme from YSU to MYJ. Then we draw an arrow from the run which uses the YSU scheme to the one that uses the MYJ scheme. If the arrow is pointing downwards it means the simulation has a lower RMSE and higher correlation coefficient compared to the default run, if it is pointing upwards it means the simulation is performing worse in these metrics. The magnitude of the arrow shows how big the increase or decrease of performance is.

In Fig. 14 it can be seen that all the arrows are pointing downwards, indicating that all simulations with the MYJ scheme have a lower RMSE and correlation coefficient than those using the YSU scheme. The magnitude of the arrow is the largest for the simulations using the 500 m horizontal grid spacing. This indicates that the MYJ scheme is particularly performing better than the YSU scheme when it is used with a relatively fine grid spacing. Furthermore it can be seen that the standard deviation is underestimated in the simulations using the MYJ scheme, whereas the simulations using the YSU scheme have a standard deviation that is slightly closer to the observed one. The underestimation of the variance of mesoscale models compared to observations was also seen in Hahmann et al. (2015) and Vincent et al. (2015) and can be attributed to the inability of the model to resolve all scales. It is possible that turning off the spectral nudging could slightly improve the under prediction in variance (Vincent et al., 2015).

To explore the effect of the other simulations, we now keep the PBL scheme the same, consider the run with a 2 km horizontal grid spacing to be the reference and draw an error from the default run to a run with a certain perturbation. The simulation YSU_{ERA} has the longest, downward pointing arrow. This shows that, when using the same PBL scheme, using ERA-interim data as

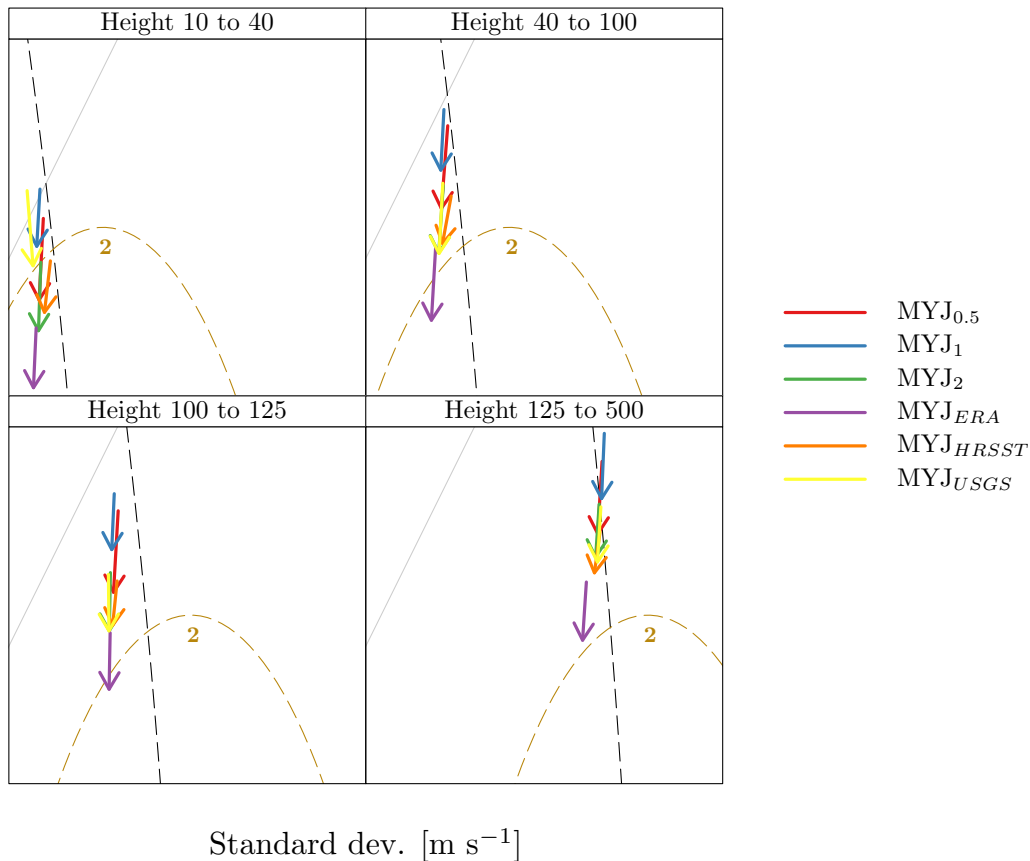


Figure 14. Taylor diagrams showing the influence of changing the PBL scheme from YSU to MYJ and keeping the rest of the model configuration constant.

boundary conditions has the largest positive impact on the model performance. The YSU₁ and YSU_{0.5} have upward pointing arrows, with the largest magnitude for the YSU₁ simulation, which shows that increasing the horizontal resolution does not improve the model performance.

The simulation YSU_{USGS} shows an upward pointing arrow at heights between 10 and 50 m, indicating that the model performance is worse using the USGS data as lower boundary condition. At greater heights, the arrow becomes smaller and between 150 and 500 m it is pointing in a downward direction. As expected this indicates that using CORINE land use data describes the terrain around the experimental site better, but at higher heights the effect of changing the lower boundary conditions is limited. Using the different description of the SST has only a very small impact on the model performance at all heights.

Figure 16 shows the change in model performance of the different runs using the MYJ PBL scheme. Generally the effect of different changes on the model performance is very similar compared to when the YSU scheme is used: MYJ_{ERA} shows the biggest model improvement and increasing horizontal grid spacing produces less skillful forecasts. The sensitivity to using the USGS data as lower boundary conditions appears to be slightly lower than with the YSU scheme, with a shorter arrow of MYJ_{USGS} in Fig. 16 than YSU_{USGS} in Fig. 15.

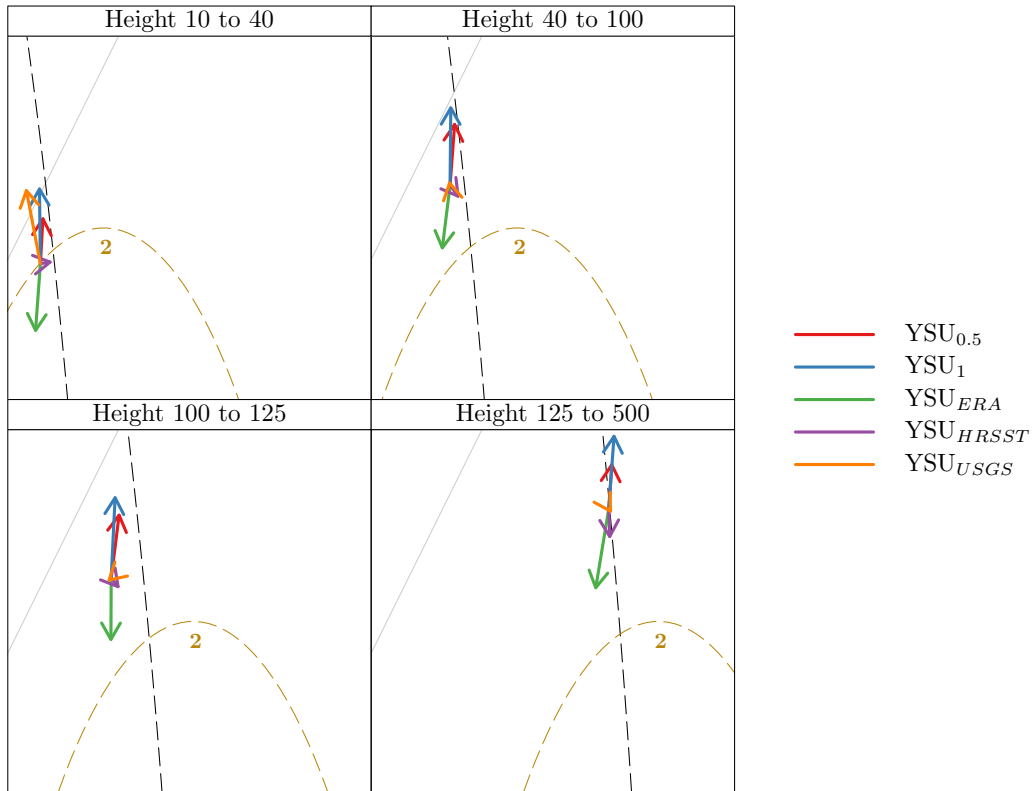


Figure 15. Taylor diagrams showing the influence of perturbing the SST, horizontal resolution, reanalysis data and land-surface scheme for the YSU scheme.

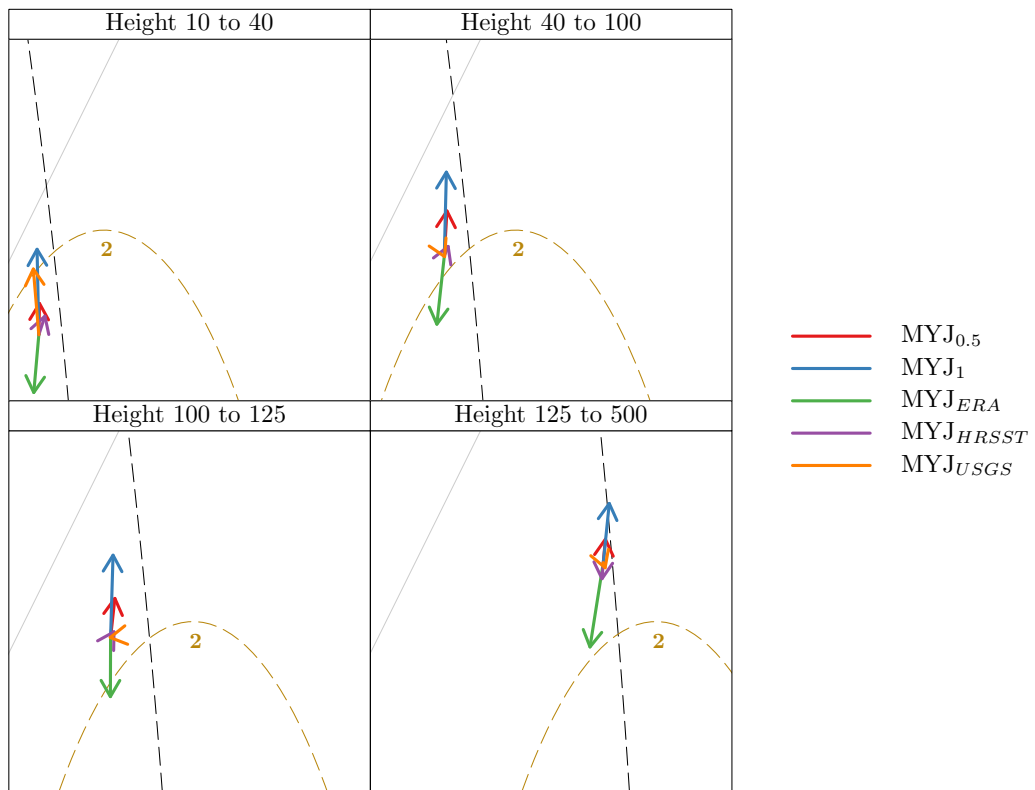


Figure 16. As Fig. 15, but using the MYJ scheme.

6 Analysis of mean wind speed during the full period

In order to understand the WRF model behavior under different resolutions and configurations we analyze the 4 month average (2 November 2015 – 1 March 2016) wind speed, which covers all of the RUNE field campaign. The WRF output is saved at a frequency of either 10-minute (for $\Delta x = 3$ km or less) or hourly (for $\Delta x = 4.5$ km or greater). The 4 month averages are made with all the available samples in most comparisons. However, for consistency in the comparison of the various resolution runs only the hourly data is used. In this section we first study the horizontal differences in mean wind speed, usually at 100 m AGL, between the various runs. Later we will compare the coastal gradient in wind speed across the transition zone from water to land and the differences in wind speed that could be expected at a single site using the WRF model output from the various simulations.

6.1 Effect of land, atmosphere and sea inputs

We compare the effect in the mean wind speed from using the two land use datasets: USGS (WRF default) versus CORINE, as discussed previously in section 3.2.3. The WRF land use maps are shown in Fig. 17. It is clear that the USGS dataset provides a simpler and smoother version of the landscape and provides much smaller cities (in purple color) than those provided by the CORINE dataset. Part of this comes from the original spatial resolution of the data: 250 m in the CORINE, versus 1 km in the USGS. However, the satellite used, periods and algorithms are different between the two datasets.

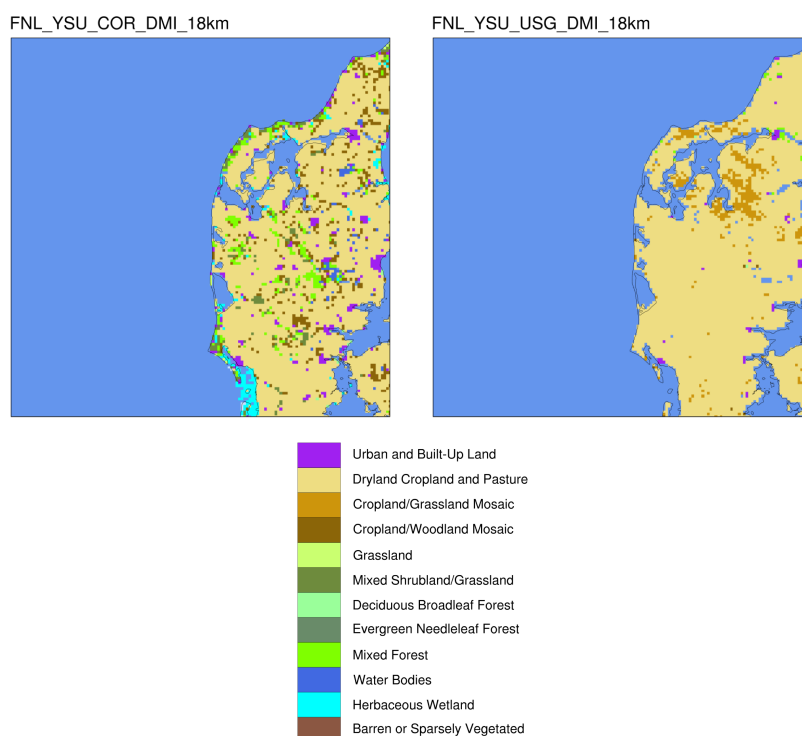


Figure 17. Land use class for the WRF inner domain ($\Delta x = 2$ km) using CORINE (left) and USGS (right) land use data.

The difference in mean wind speed at 100 m AGL obtained by using the two land use maps with the two PBL schemes is shown in Fig. 18. It is clear that the largest differences occur in

regions where pasture or agricultural areas are replaced by forest, with an associated change in surface roughness length from 5 cm to 50 cm for mixed forest and 90 cm for forest. It is interesting to see that the response to the roughness change is larger for the MYJ scheme (max wind speed difference of -1.14 m s^{-1}) than for the YSU scheme (max wind speed difference of -0.98 m s^{-1}). When one zooms in into the inner RUNE region (Fig. 19 with a different color label) it is possible to see that the effect of the rougher land extends also offshore. This extension is much larger when using the MYJ scheme than the YSU scheme.

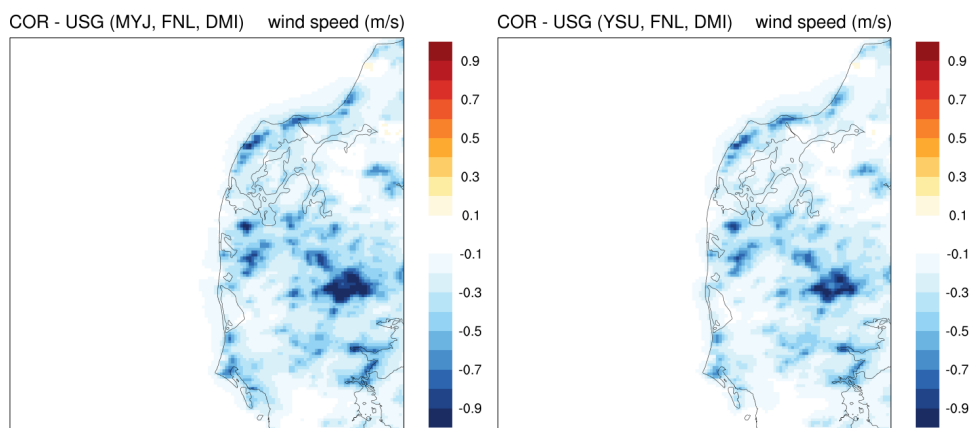


Figure 18. Mean wind speed difference (m s^{-1}) at 100 m AGL resulting from using CORINE and USGS land use and two PBL schemes: MYJ (left), YSU (right). Runs use FNL forcing, DMI SST and $\Delta x = 2 \text{ km}$ grid spacing.

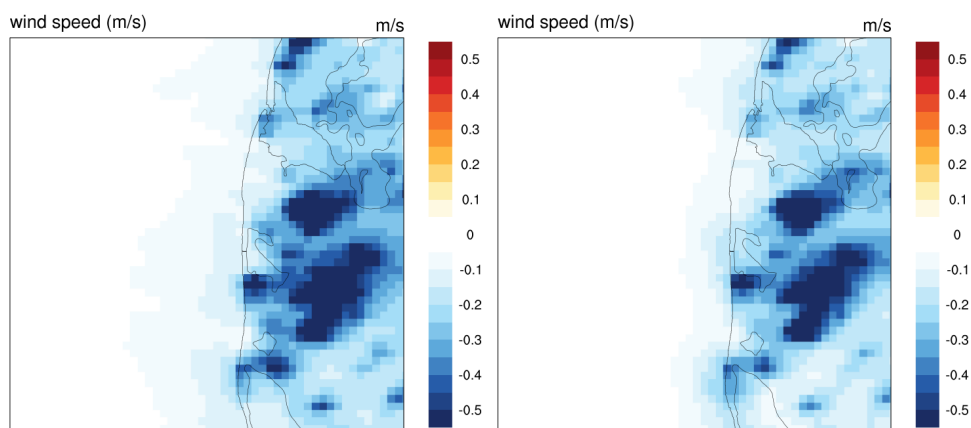


Figure 19. Mean wind speed difference (m s^{-1}) at 100 m AGL resulting from using CORINE and USGS land use and two PBL schemes: MYJ (left), YSU (right). Zoom into the RUNE inner region (D4). Note the different color scale than in Fig. 18. Runs use FNL forcing, DMI SST and $\Delta x = 2 \text{ km}$ grid spacing.

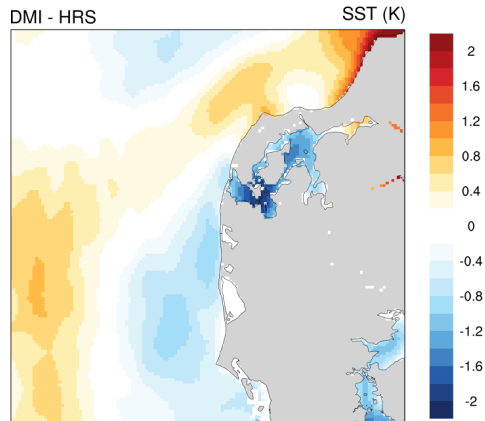


Figure 20. Mean SST difference (K) from the DMI and HRSST as interpolated to the WRF inner domain at a $\Delta x = 2$ km grid spacing.

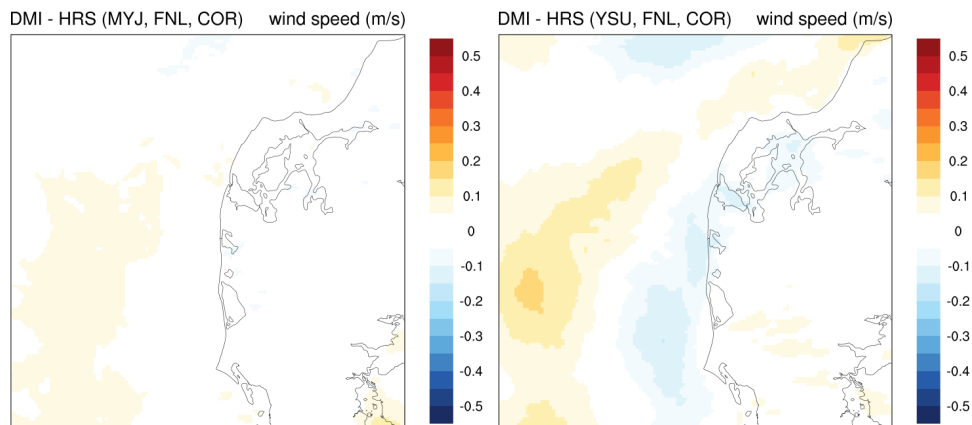


Figure 21. Mean wind speed difference ($m s^{-1}$) at 100 m AGL resulting from using SST from DMI and HRSST and two PBL schemes: MJY (left), YSU (right). All runs use the FNL forcing and $\Delta x = 2$ km grid spacing.

The difference in the 4-month mean SST between the DMI data and HRSST data is shown in Fig. 20 as interpolated to the WRF inner domain. SSTs are colder in the DMI dataset near the coast but warmer in band further offshore. The difference in mean wind speed which results from the different SST source is presented in Fig. 21 for the two PBL schemes. Here a much stronger response is seen under the YSU scheme (right plot) than the MYJ scheme (left plot). Differences are small with a absolute maximum difference when using the YSU scheme of $\pm 0.16 m s^{-1}$. The differences in wind speed coincide geographically very well with those in SST, with warmer SST resulting in higher wind speeds, and vice versa, but mostly when using the YSU scheme (right panel).

Finally we investigate the effect of the atmospheric forcing. We compare the mean wind speed simulated by the WRF model using either FNL and ERA Interim atmospheric initial, boundary and data for nudging. The differences in the 100 m AGL mean wind speed are shown in Fig. 22. The spatial pattern of differences in mean wind speed is similar between the two PBL schemes, with large positive differences ($\geq 0.4 m s^{-1}$) in the south-west sector of the domain to negative

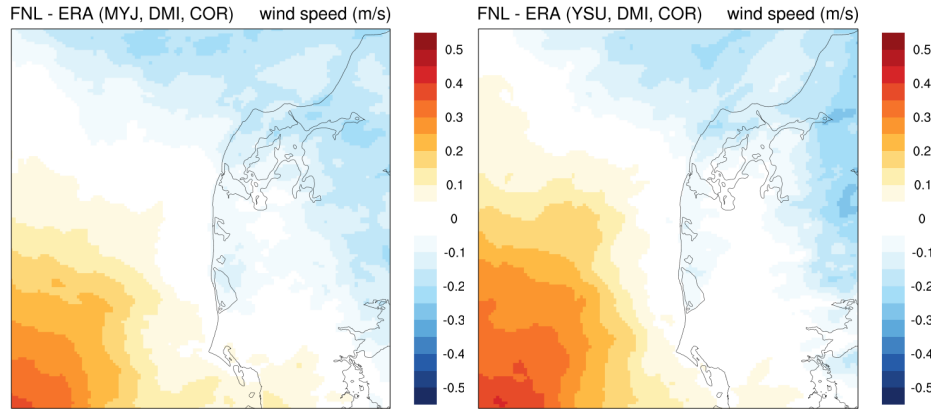


Figure 22. Mean wind speed difference ($m s^{-1}$) at 100 m AGL resulting from using FNL or ERA Interim forcing and two PBL schemes: MJY (left), YSU (right). All runs use CORINE landuse, DMI SSTs and $\Delta x = 2$ km grid spacing.

differences ($\leq -0.25 m s^{-1}$) in the north-east sector. Differences are larger further offshore in the simulation using the YSU scheme (right panel) than in that using the MYJ scheme. The same pattern of differences in wind speed does not exist in the reanalysis themselves; the origin of the differences is unknown.

6.2 The effect of resolution

We compare here the effect of the WRF model spatial grid spacing on the wind climate estimation. Figures 23 and 24 show the mean wind speed simulated by WRF for various grid spacings (from 6 km to 0.5 km) using the MYJ and YSU PBL schemes. It is possible to see from these runs that over the sea isolines of a certain wind speed (called isotachs) match relatively well geographically between the various grid spacings. The only evident feature is that the isotachs are smoother in the simulations with coarser grid spacings than in the finer ones. However, it is worth noting that in the 0.5 km grid spacing the higher wind speed isotach bends close to the western boundary under both PBL schemes. This is likely a consequence of the edge of the D4 domain. To investigate this coastal gradient in more detail we will examine cross sections of wind speed along the coast in the following section (section 6.3). Over land, where the details of land use (see Fig. 3) and associated larger surface roughness length appear as the spatial resolution increases, wind speeds are reduced.

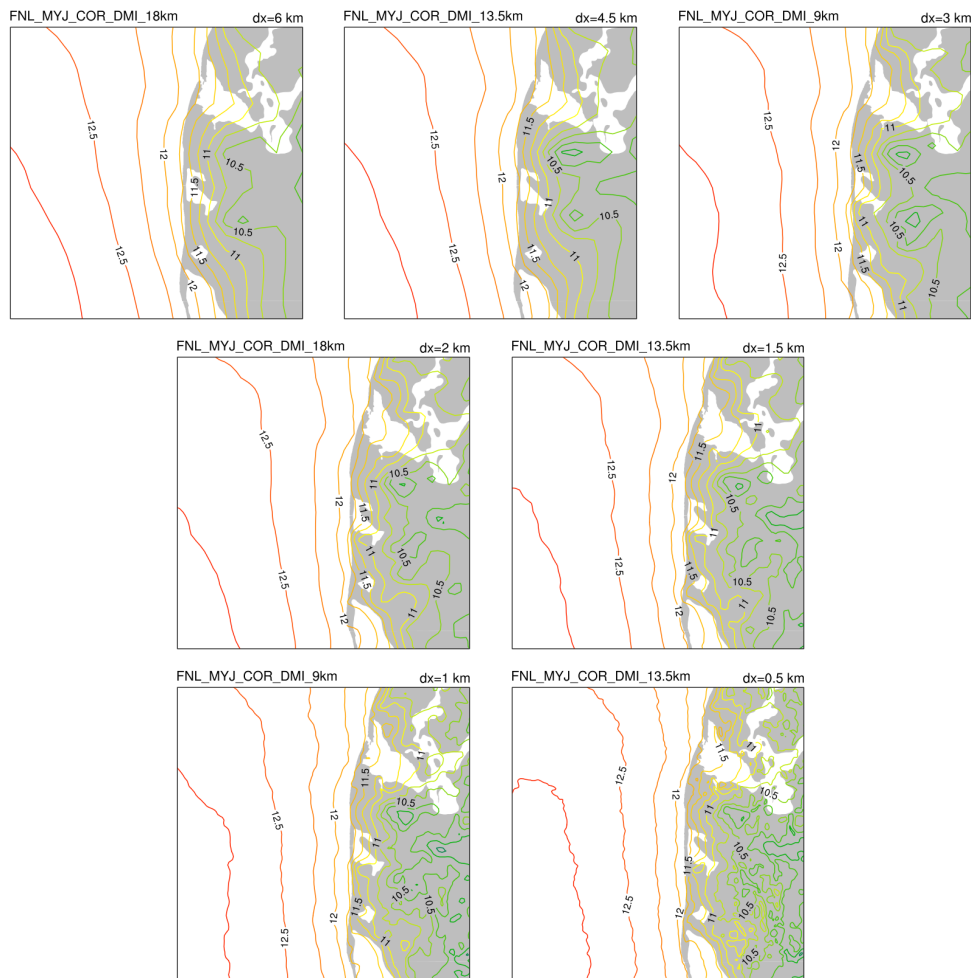


Figure 23. Mean wind speed ($m s^{-1}$) at 100 m AGL resulting from various model resolutions from top to bottom and left to right: 6 km (D2), 4.5 km (D2), 3 km (D2), 2 km (D3), 1.5 km (D3), 1 km (D3) and 0.5 km (D4). All simulations use the FNL forcing, CORINE landuse, DMI SST and MYJ scheme. All plots cover the D4 domain.

It is also interesting to examine the effect of the two different PBL schemes in the simulated WRF mean wind speed as a function of the spatial grid spacing. This is shown in Fig. 25. The pattern of differences is similar in all grid spacings with a minimum difference in wind speed around the coastline that increases west to the center of the North Sea and east to land. This

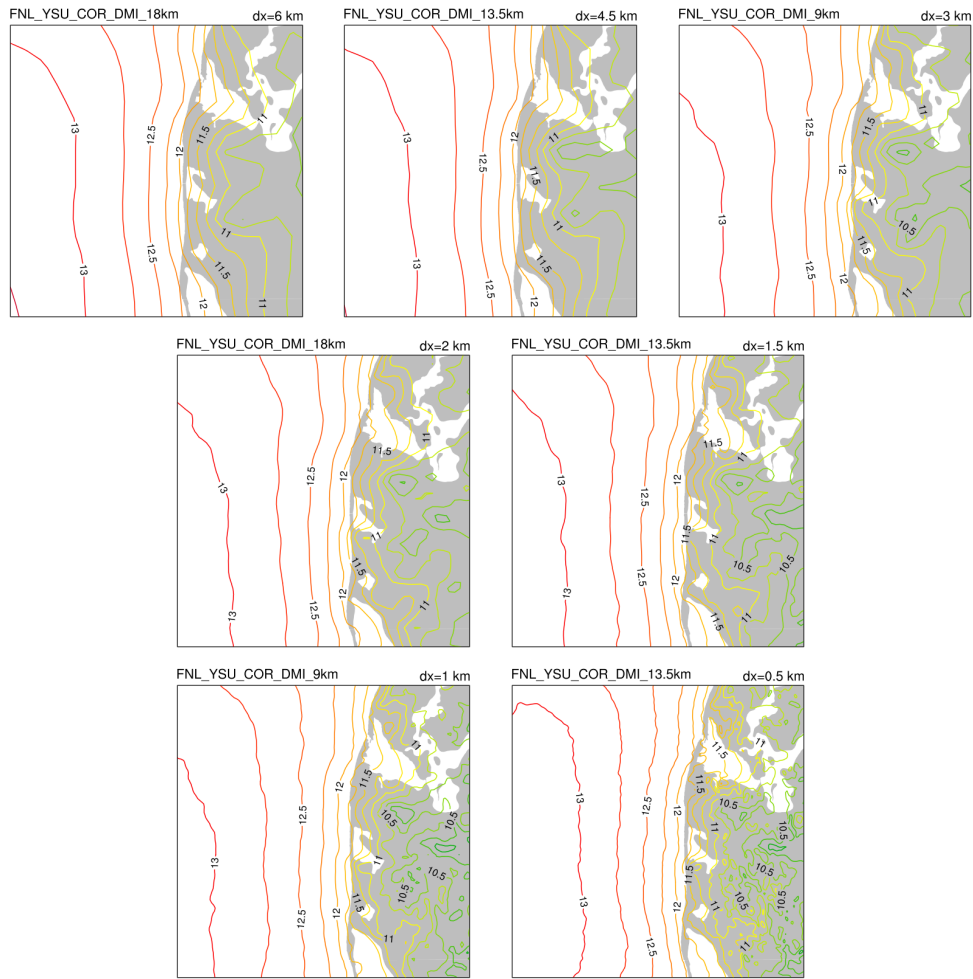


Figure 24. Mean wind speed ($m s^{-1}$) at 100 m AGL resulting from various model resolutions from top to bottom and left to right: 6 km (D2), 4.5 km (D2), 3 km (D2), 2 km (D3), 1.5 km (D3), 1 km (D3) and 0.5 km (D4). All simulations use the FNL forcing, CORINE landuse, DMI SST and YSU scheme. All plots cover the D4 domain.

pattern reflects a difference in the coastal gradient of the mean wind. The effect is a little more pronounced in the finer grid spacings. Also, the differences are smaller in the 9/3/1 km simulation (e.g. 3 km and 1 km) than in the other two model configurations. We speculate that it could be due to the large ‘jump’ in resolution from the FNL analysis ($1/4^\circ$, ~ 30 km) to the outer 9 km WRF grid.

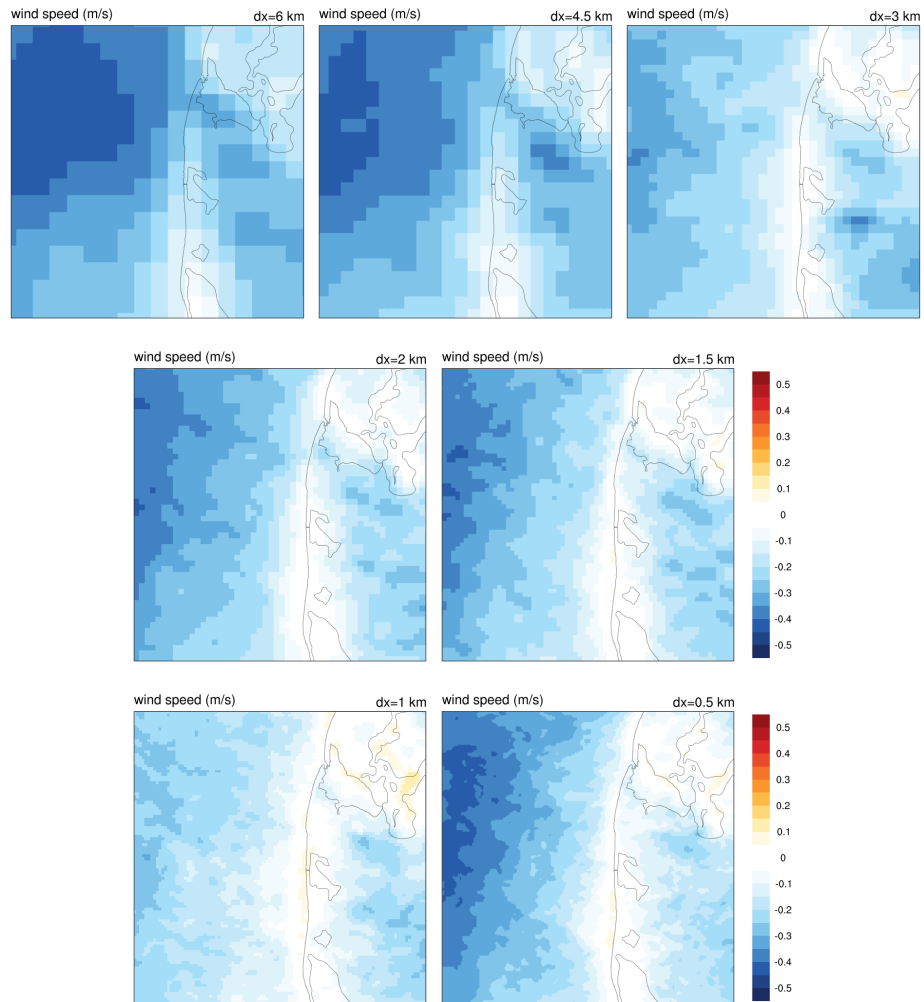


Figure 25. Difference in mean wind speed ($m s^{-1}$) at 100 m AGL resulting between the simulation using MYJ and PBL schemes at the various model resolutions: 6 km (D2), 4.5 km (D2), 3 km (D2), 2 km (D3), 1.5 km (D3), 1 km (D3) and 0.5 km (D4). All simulations use the FNL forcing, CORINE landuse and DMI SST; all plots cover the D4 domain.

Figures 26 and 27 show the variance of the wind speed calculated using the hourly sample for all WRF model grid spacings and the two PBL schemes. The pattern of wind speed variance is very similar: larger values over the sea, smaller values over land, with countours of equal variance more of less parallel to the coastline. Here there is a dramatic difference in the variance of the wind speed between the WRF simulations using the MYJ and the YSU scheme. When using the MYJ scheme the largest values are $\sim 30 \text{ m}^2 \text{ s}^{-2}$, while in the YSU runs values are above $36 \text{ m}^2 \text{ s}^{-2}$ away from the coast in all the simulations. Values over land are also larger in the simulations using the YSU scheme than those using the MYJ scheme.

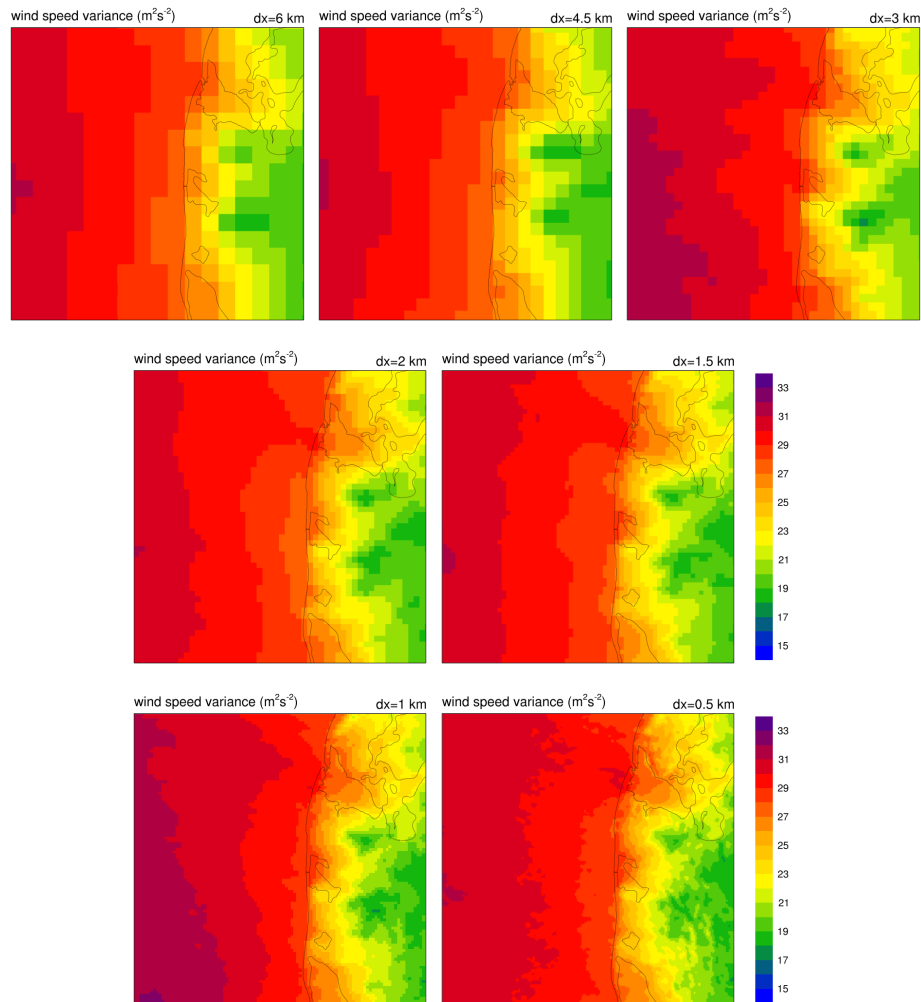


Figure 26. Variance in the mean wind speed ($\text{m}^2 \text{ s}^{-2}$) at 100 m AGL from the simulation using the MYJ PBL scheme at the various model resolutions: 6 km (D2), 4.5 km (D2), 3 km (D2), 2 km (D3), 1.5 km (D3), 1 km (D3) and 0.5 km (D4). All simulations use the FNL forcing, CORINE landuse and DMI SST; all plots cover the D4 domain. Hourly sampling is used in all the calculations.

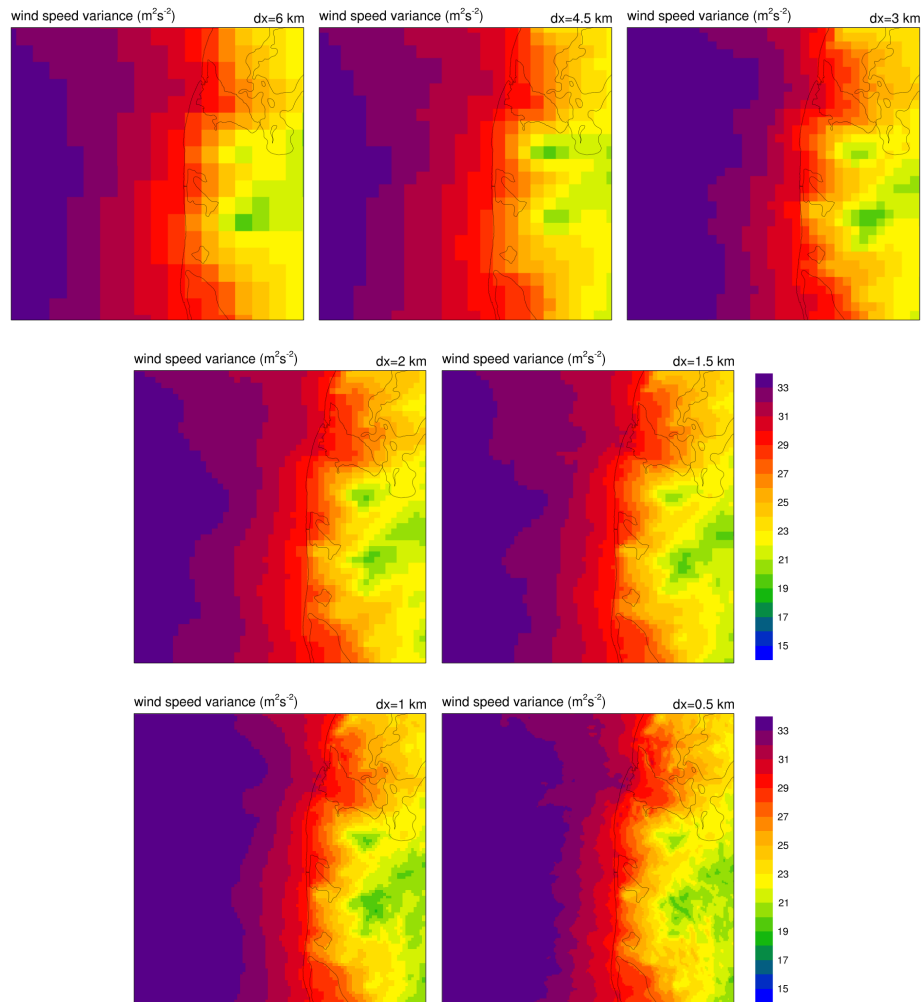


Figure 27. Variance in the mean wind speed ($m^2 s^{-2}$) at 100 m AGL from the simulation using the MYJ PBL scheme at the various model resolutions: 6 km (D2), 4.5 km (D2), 3 km (D2), 2 km (D3), 1.5 km (D3), 1 km (D3) and 0.5 km (D4). All simulations use the FNL forcing, CORINE landuse and DMI SST; all plots cover the D4 domain. Hourly sampling is used in all the calculations.

6.3 Examining the coastal gradient

To focus attention on the gradient in wind speed along the coastal transition from water to land, we examine cross sections of mean wind speed at the latitude of the WRF mass grid point closest to the Vara lidar latitude ($\approx 56.498^\circ\text{N}$) which will vary slightly as a function of the model grid spacing, from 56.4188° to 56.4730°N . The position of the coastline in the WRF model grid used to align the WRF-simulated cross sections is determined by the average longitude between the center of the last water point and the center of the first land grid point.

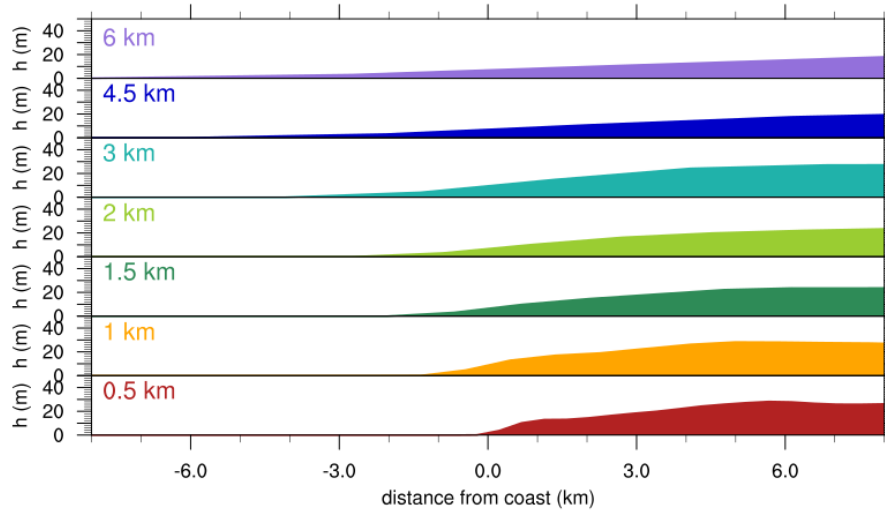


Figure 28. Terrain elevation (m) across the coastal transition centered at the Vara latitude for the various WRF resolutions.

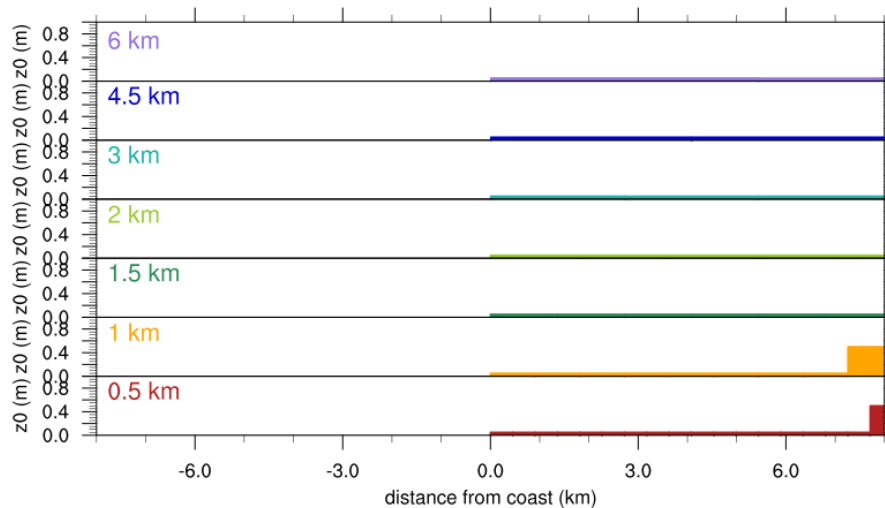


Figure 29. Surface roughness length (m) across the coastal transition centered at the Vara latitude as a function of distance to the WRF coast for the various WRF resolutions.

Figure 28 shows the surface terrain elevation for the various WRF grid spacings aligned by the distance to the coastline. It is evident that only at the higher grid spacing ($\Delta x = 0.5$ km) the terrain starts resembling that of the escarpment shown in the real topography. The surface roughness length in Fig. 29 is comparable and well represented in all the WRF runs with relatively smooth Dryland cropland and pasture ($z_0 = 0.03$ m).

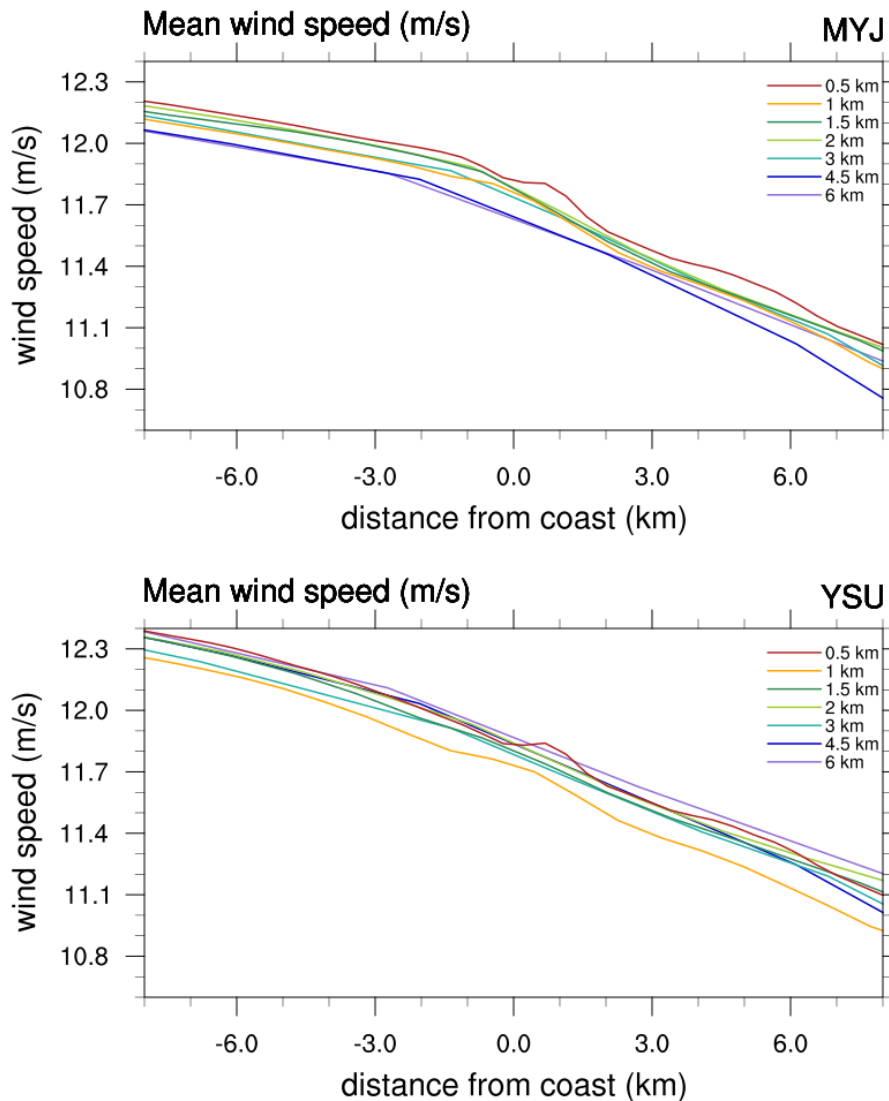


Figure 30. Mean wind speed at 100 m AGL for the MYJ (top) and YSU (bottom) PBL schemes as a function of distance to the WRF coast for the various WRF resolutions. Colors are as in Figs. 28 and 29.

The gradient of mean wind speed along the coastal transition is shown in Fig. 30 for the various WRF grid spacings using the MYJ and YSU PBL schemes. In the gradients for the MYJ scheme (Fig. 30 top), the wind speed tends to be lower for the lower resolution run, and more or less increases with decreasing grid spacing, but the differences are $\leq 0.15 \text{ m s}^{-1}$ at a distance of 8 km offshore from the coast. At this distance the YSU simulations show similar spread, but the mean wind speed is a bit higher than in the simulations using the MYJ scheme. In the simulations using the YSU scheme the lowest wind speed is that of the $\Delta x = 1.0 \text{ km}$. It is perhaps more interesting to compare the slope of the mean wind speed for the WRF simulations using the two PBL schemes. For the MYJ scheme the various curves have similar slope and experience a similar change of slope after the coastline. That is the winds decrease in speed slower before the coast than afterwards. In the YSU schemes this slope is sharper and almost identical before and after the coastline. A couple of small "bumps" in the mean wind speed are seen in the $\Delta x = 0.5 \text{ km}$ simulation, which is associated with higher terrain at the coastline and further inland.

Figure 31 shows the differences in the simulated wind speed across the coastline for the various WRF setups in the $\Delta x = 2 \text{ km}$ simulations. Here again we see the separation of the MYJ-based

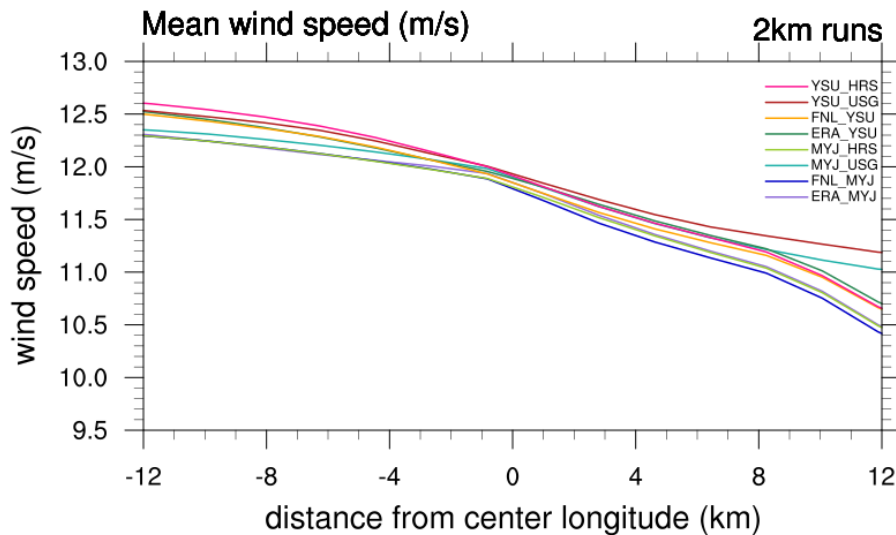


Figure 31. Mean wind speed at 100 m AGL for all the $\Delta x = 2$ km as a function of distance to the WRF coast for the WRF configurations in the $\Delta x = 2$ km simulations.

and YSU-based runs offshore away from the coast. All runs seem to converge to a similar value right before the coastline. As expected from the low surface roughness length, the two simulations using the USGS land use show much larger wind speeds inland.

The previous comparison shows how insensitive the model is to the various grid spacings and the various special model setups. However, these cross-sections are centered on the RUNE Vara location, where the model grid was centered and specially selected because of the straight North-South position of the coastline. To investigate how the model results compare at a more complex location, Figs. 32 are sections along $56^{\circ}56'N$. Here the differences in wind speed due to differences in the position of the coastline and in surface roughness length over land are evident. It is also interesting to note that the spread in the mean wind speed is larger among the resolutions in the runs using the YSU than in those using the MYJ scheme.

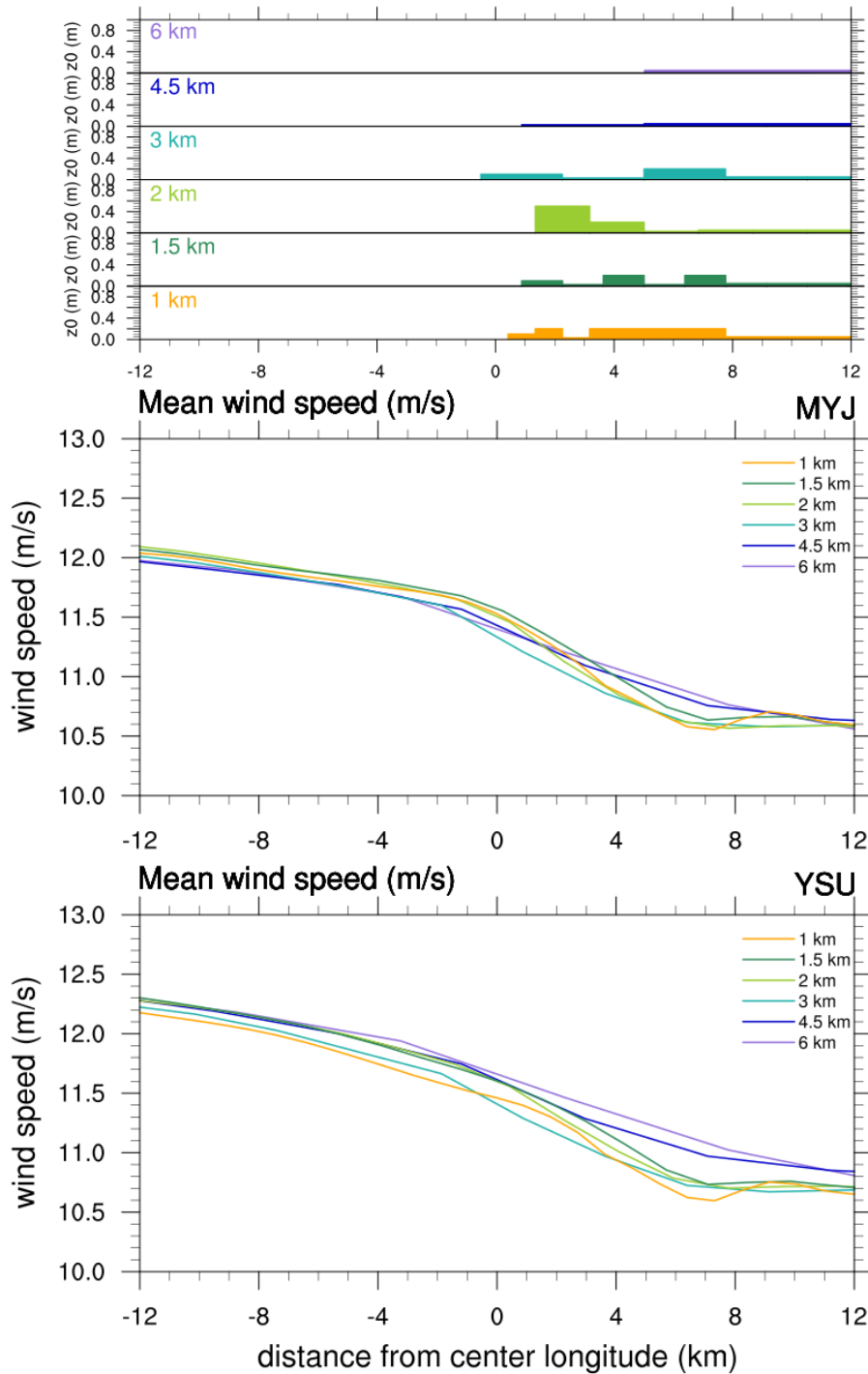


Figure 32. Surface roughness length (m; Top) and mean wind speed at 100 m AGL for the MYJ (middle) and YSU (bottom) PBL schemes across the coastal transition at $56^{\circ}56'N$ as a function of distance to the real coast for the various WRF resolutions. Colors are as in Figs. 28 and 29.

Finally we compare the effect of the various model setups and spatial grid spacings on the wind speed distribution at a single point some distance from the coast. This is shown by box plots on Fig. 33. A ‘box’ plot shows the first, median and third quartiles by lines on the box and the upper and lower whiskers show the maximum and minimum values; the dot shows the average wind

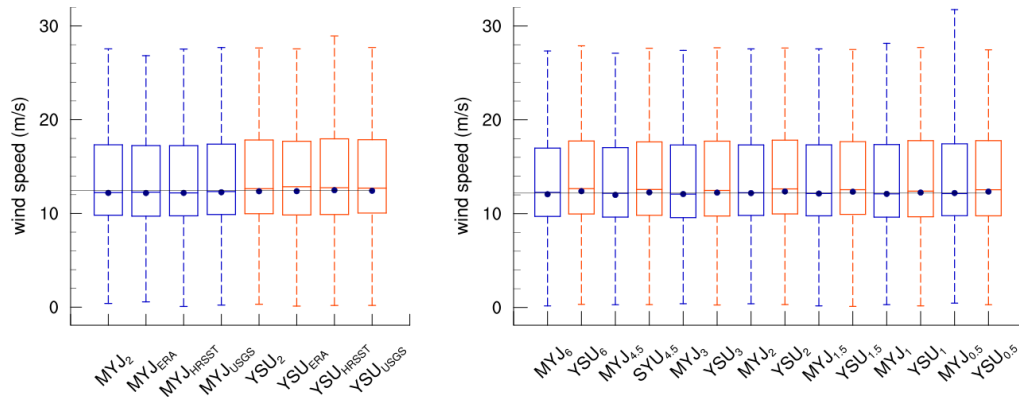


Figure 33. Box diagram showing the statistics of the wind speed at 100 m AGL at a point located 8km west from the coast (7.99090° E 56.49785° N) for the various $\Delta x = 2$ km runs (left) and the various WRF model grid spacings (right).

speed. In the $\Delta x = 2$ km simulations all 10-min values are used; in comparison of the various resolutions we use the hourly wins speed values.

The figure shows very similar distributions for all the simulations and WRF model setups. No systematic increase or decrease in the mean wind speed with increased horizontal wind spacing is apparent in the simulations. The only difference is slightly wider distributions in the simulations using the YSU than the MYJ schemes, which is relevant later in the calculation of the mean power density in Table 6. The only "anomaly" is the considerably larger maximum wind speed in the $\Delta x = 0.5$ km using the MYJ scheme.

6.4 Satellite-derived maps

The description of the satellite data collected and used during the measurement campaign is available in Floors et al. (2016a). The mean wind speed derived during the RUNE campaign (November 1st 2015 to February 29th 2016) of ASCAT L3 wind speed retrievals is shown in Figure 34 (left panel). Wind speeds at 10 m above the surface range from, approximately, 11 m s^{-1} offshore to 10 m s^{-1} at the grid point offshore from Vara's location. This range is lower than what has been previously shown from the model results by approximately 1 m s^{-1} , and it can be due to the height difference, as lower wind speeds are expected closer to the surface. Nonetheless, a 1 m s^{-1} gradient from offshore towards the coast is identified, in alignment with modelled winds. The higher winds further offshore are also reproduced using the WRF model simulations (see Fig 23). The data availability decreases when approaching the coastline, from 250 wind retrievals offshore, to approximately 70 at the grid point offshore from Vara.

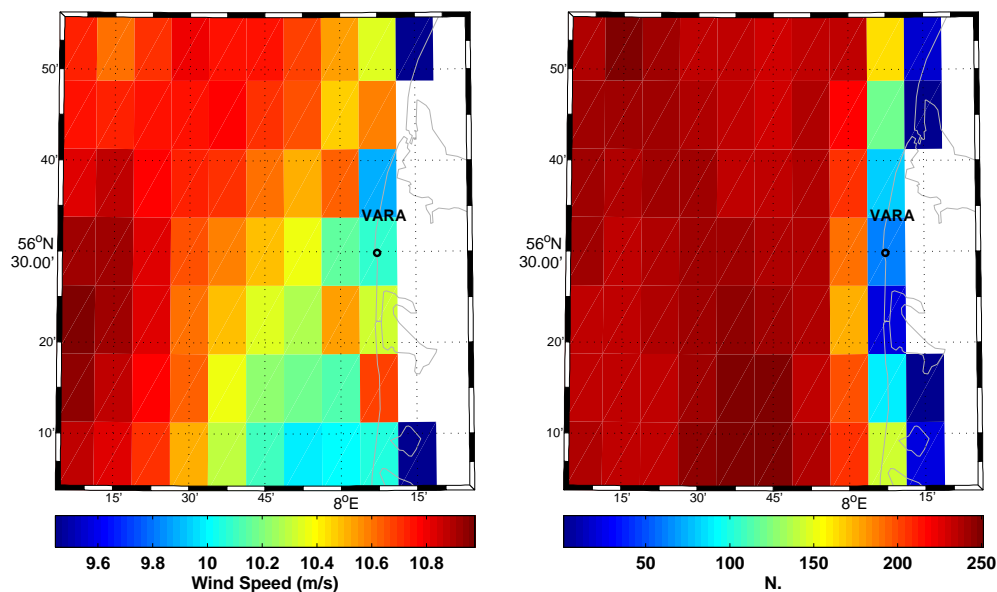


Figure 34. Mean wind speed (left), where the data availability (right) is higher than 10, over the RUNE area for the entire period of the measurement campaign (Nov 1st 2015 - Feb 29th 2016), based on the ASCAT L3 product.

The dominant wind direction patterns at 10 m above the surface, as captured by ASCAT, are shown in Fig. 35, obtained from the grid cell closest to Vara (right) and the one further offshore (left). The dominant wind direction from the point closest to Vara is from the South, with some westerly winds also appearing. When examining the grid cell further offshore, approximately 13 km away, the dominant wind direction is from the West and South-West.

Figure 35 also shows the corresponding wind roses extracted from the WRF model simulations for the points closest to the ASCAT points and for the same times as the overpass ASCAT times (middle) or for the full WRF modelling period (bottom). The MYJ_{ERA} set-up is used. The WRF model results for the grid point 13 km away from Vara (left column) are in agreement with the ASCAT findings, independent of the sample size (189 or 17424). The WRF model results for the grid point closest to Vara (right column), are in agreement with the ASCAT findings regarding the dominant wind direction (middle) when the same time sampling is used. When all the available WRF outputs are used, the dominant wind direction changes from southerly to south-westerly. This indicates that the ASCAT sampling may not be sufficient to represent the wind characteristics at such a close distance from the land, and WRF is able to reproduce this sampling-related variability so close to the land.

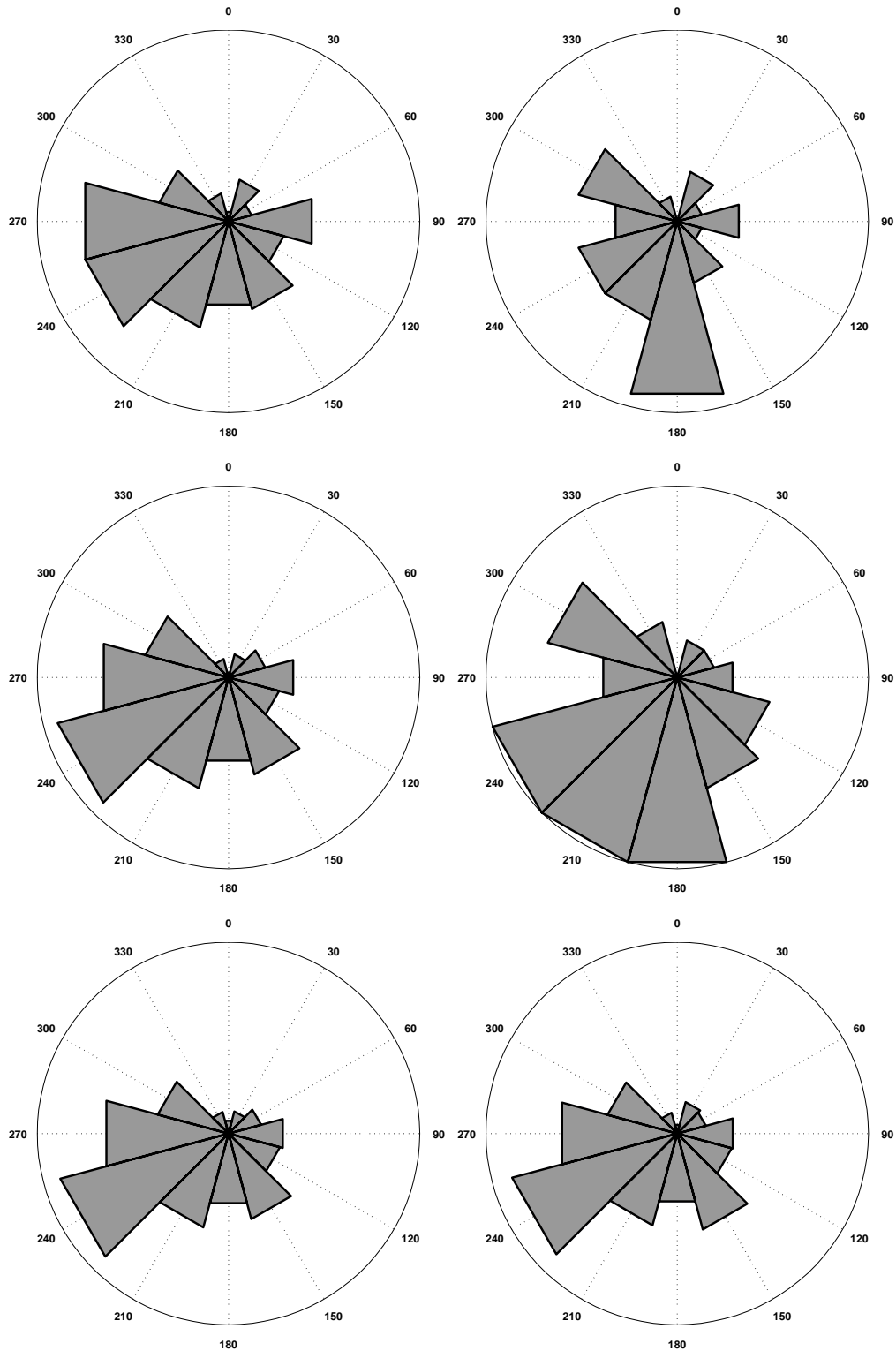


Figure 35. Top: Wind roses from the ASCAT grid cell closest to Vara (right), with its center at a distance of ~ 7.5 km away from the shore. A total of 63 retrievals are available. Wind rose from one grid cell further, at a distance of ~ 13 km from the shore (left) with a total of 189 retrievals available. Middle: Corresponding wind roses for the same points and times as ASCAT, but from the MYJERA simulations. Bottom: Same as middle, but for all available hourly WRF outputs.

7 Offshore wind resource estimation

Wind resource assessment are usually recommended to have at least a full year of measurements to represent the long-term wind resource and to avoid seasonal biases. However, due to the limited time of the RUNE campaign we first compare limited data sets where simulation results were obtained concurrent with the available measurements. The wind speed derived from the dual and PPI setup were retrieved for a distance of ≈ 1 and 5 km offshore and compared with the concurrent wind speeds derived from the closest point in the model set-up (Table 6). The power density, $P = 0.5\rho U^3$, was computed using a standard air density of $\rho = 1.2 \text{ kg m}^{-3}$ for each 10-min interval.

	Location (m)	N	Wind speed		
			50 m	100 m	150 m
YSU _{ERA}	-920.00	2936	11.84 (-0.3)	13.20 (+1.1)	14.15 (+0.9)
MYJ _{ERA}	-920.00	2936	11.88 (+0.0)	13.26 (+1.5)	14.15 (+0.9)
Dual setup	-1520.00	2936	11.88 (+0.0)	13.06 (+0.0)	14.03 (+0.0)
PPI	-1600.00	2936	11.94 (+0.5)		
YSU _{ERA}	-4940.00	94	13.85 (+2.1)	14.90 (+3.3)	15.89 (+3.3)
MYJ _{ERA}	-4940.00	94	13.61 (+0.3)	14.63 (+1.5)	15.73 (+2.3)
Dual setup	-4990.00	94	13.57 (+0.0)	14.42 (+0.0)	15.38 (+0.0)
PPI	-5000.00	94	14.10 (+3.9)	14.92 (+3.5)	15.80 (+2.7)

	Location (m)	N	Power density		
			50 m	100 m	150 m
YSU _{ERA}	-920.00	2936	1387 (- 3.2)	1899 (+ 0.8)	2338 (- 0.1)
MYJ _{ERA}	-920.00	2936	1405 (- 1.9)	1920 (+ 2.0)	2331 (- 0.4)
Dual setup	-1520.00	2936	1433 (+ 0.0)	1884 (+ 0.0)	2340 (+ 0.0)
PPI	-1600.00	2936	1439 (+ 0.4)		
YSU _{ERA}	-4940.00	94	1767 (+ 7.2)	2196 (+11.5)	2679 (+12.2)
MYJ _{ERA}	-4940.00	94	1665 (+ 1.0)	2070 (+ 5.1)	2585 (+ 8.2)
Dual setup	-4990.00	94	1649 (+ 0.0)	1969 (+ 0.0)	2388 (+ 0.0)
PPI	-5000.00	94	1843 (+11.8)	2189 (+11.1)	2591 (+ 8.5)

Table 6. The wind speed and power density at two locations and 3 heights from the dual set-up, PPI set-up and two model set-ups. The numbers denoted the wind speed (m s^{-1}) and power density (W m^{-2}). The relative difference in per cent compared to the observations of the dual setup is given in brackets. The location is given relative to the position of Vara (pos. 2) and is negative towards the west. The number of available 10-min observations is denoted as N .

Only the model simulations using the ERA-interim data are shown, because they performed best in the model evaluation in Sect. 5.3. Due to the coarse resolution of the WRF simulations the closest grid point is 600 m away from the dual setup sampling point at 1.5 km offshore. It can be seen that at the position close to the coast (first four rows) the number of available measurements is much higher than at 5 km offshore. The observed wind speed is very close to the modelled wind speed at all heights and the relative differences are $\approx 1 \%$. For the other model setups the relative error was between 0 and 3 % (not shown). The wind speed derived from the PPI setup is very close to that obtained from the dual setup for this position.

At ≈ 5 km offshore, the model simulations over predict the mean wind speed by $\approx 0.5 \text{ m s}^{-1}$ ($\approx 1\text{-}3 \%$) at all heights for the 94 available 10-minute intervals. The mean wind speed obtained from the PPI setup is $\approx 3 \%$ higher than that from the dual setup. This can be related to the inability of the PPI setup to reconstruct the wind speed when the radial wind speed is near zero, i.e. for northerly and southerly winds. This issue is further discussed and illustrated in Floors et al. (2016b).

The power density near the coast is also well represented in the model simulations compared to the dual setup measurements, with a relative bias of $< 3\%$. At ≈ 5 km offshore, the simulations using the YSU scheme over predict the power density significantly at 100 and 150 m with a relative error of $> 10\%$. The power density obtained from the PPI setup is higher than that observed from the dual setup.

To obtain a data set that is more representative for the simulation period, we use wind speeds from all vertical profiling lidars on land. The floating lidar buoy is not used due to the limited data availability. Combining all profiling lidars results in a data set with 6544 10-min mean measurements. We then perform a WASP analysis using the wind measurements at different heights and predict the wind at a typical hub height of 100 m and compare the results with the matching 10-min model output from the model simulations (Fig. 36). The spread of the model simulations can then be considered an estimation of the model uncertainty in performing a wind resource assessment.

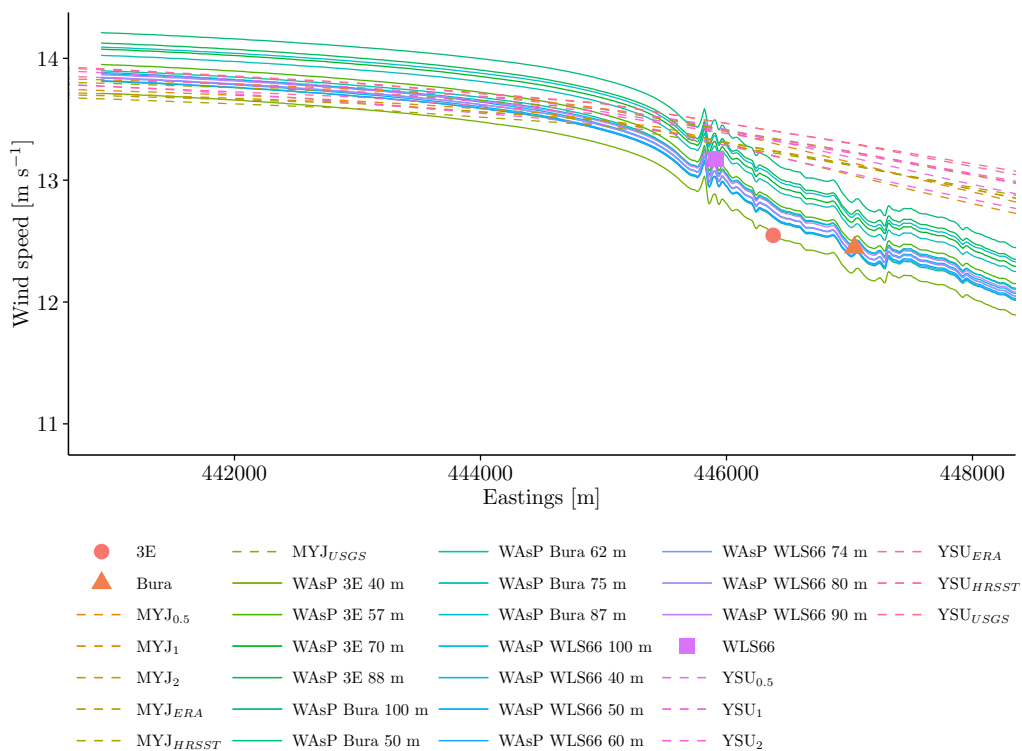


Figure 36. The mean wind speed at 100 m during the period when the vertically profiling lidars on land were available (points) from WASP estimations (solid lines) and WRF simulations (dashed lines).

It can be seen that the WASP model is rather sensitive to the height which is used to predict the wind speed. WASP simulations using the different input data do not coincide at 5 km offshore ($x = 441000$ m), but are spread between $13.7\text{--}14.2$ m s^{-1} . The different model set-ups from the WRF model have a smaller spread at that location from $13.7\text{--}13.9$ m s^{-1} , showing that it is less sensitive than WASP to estimate the offshore wind speed. However, the high spread of the WASP estimations could partially be a result of a misrepresentation of the wind shear caused by a mean stability regime that is different from the default one. This could be easily changed by choosing the heat flux parameters such that the modelled wind profile fits the observed one at a certain lidar. It can be seen that most of the WASP model estimations are closer to the observed mean wind speed inland and resolve an orographic speed-up near the coast that is not apparent in the WRF model simulations. The WRF model appears to over estimate the mean wind speed inland,

although this can also be caused by the measurement from lidar Bura and 3E which are not at the same north-south position as the simulations and the other observations.

When measurements are used to estimate the wind resource, they should give an unbiased estimation of the measured wind speed. However, Gryning et al. (2016) showed that filtering lidar data by using CNR thresholds can result in apparent higher mean wind speeds, because of the relation between aerosol conditions, CNR threshold and mean wind speed. To investigate if this problem is also present when using the long-range scanning lidars, we here do not vary the CNR threshold, but instead vary the distance up to which we include measurements that fulfill the CNR threshold.

Because the availability of 10-min intervals that fulfill the CNR requirements drops with distance (Table. 3), we expect to include measurements at long distances only when there is atmospheric conditions with many aerosols, which are most frequently observed with high wind speed conditions. In Fig. 37 transects of mean wind speeds were selected where all sampling points at 100 m fulfilled the CNR threshold up to a certain distance between 200–5000 m. The WRF model output from different set-ups is filtered by matching the 10-min intervals where the dual setup is available up to 200 m, i.e. with a minimum loss in data due to filtering. It can be seen that increasing the distance up to which the CNR threshold is applied, gives on average a higher wind speed in the transects that are left after filtering. For example at $x \approx 445000$ m, the mean wind speed increases from ≈ 12 to 13 m s^{-1} when increasing the filtering distance from 1000 to 5000 m. The same was observed for the sector scan setup, but with a smaller increase in mean wind speed (not shown). This is probably because the path length of the laser beams of the dual setup is increasing faster than that of the sector scan when moving along a line in the west-east direction.

For a wind resource estimation offshore this would imply that only lidars that have a laser power high enough to measure nearly 100% of the time will give an unbiased estimation of the mean wind speed. Filtering data with any CNR threshold will decrease the number of low wind speed estimations and thereby increase the apparent mean wind speed after filtering. More research is required to investigate if this effect can be corrected. Unfortunately there is no reliable estimation of the mean offshore wind speed during the full four-month measuring period, because the floating lidar buoy did not measure for nearly two months. Although all comparisons between the instruments deployed during RUNE showed very good agreement, careful filtering of the data is thus important for the wind resource estimation.

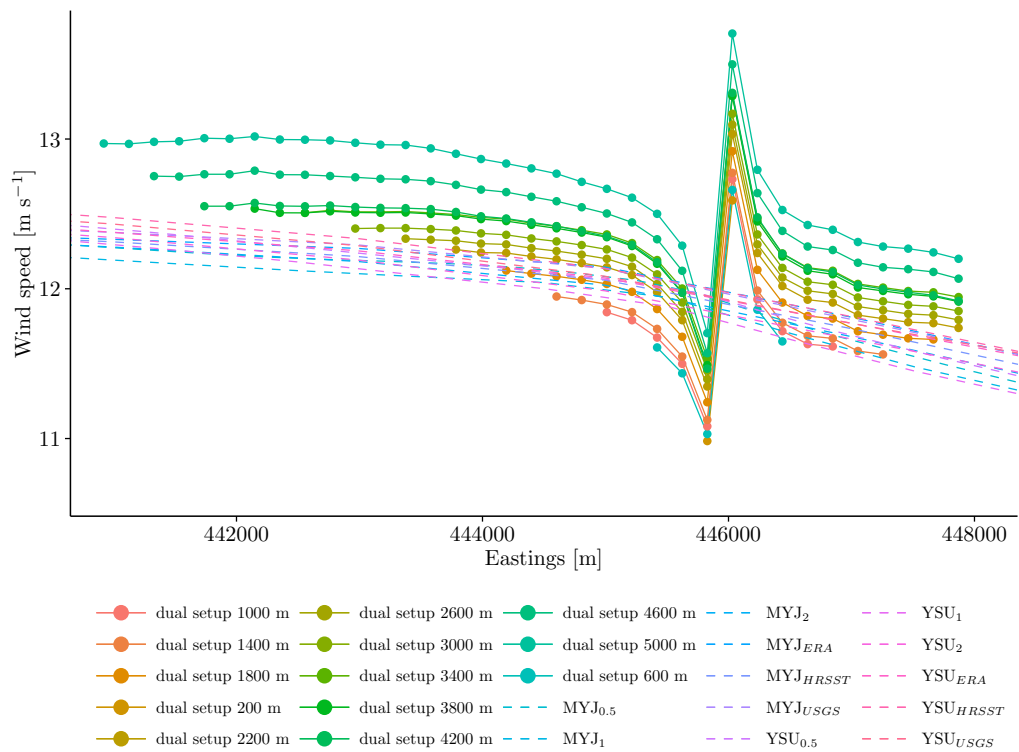


Figure 37. The mean wind speed at 100 m measured by the dual setup including measurements fulfilling the CNR criteria up to distances 200–5000 m and the modelled mean wind speed using different set-ups for the period where the dual setup filtered up to 200 m was available.

8 Summary and recommendations

The wind resource in the coastal zone was studied using mesoscale model simulations and measurements from the RUNE campaign during a four month period from November 2015 to February 2016. The WRF mesoscale model was set up in twelve different configurations. The sensitivity to the planetary boundary layer parametrization was studied by using two schemes and performing six additional sensitivity experiments to each of them. Firstly, the influence of the land cover description was investigated by using the USGS and CORINE data as lower boundary conditions. Secondly, two sources of sea surface temperatures were used to investigate the influence on offshore stability and the wind speed. Thirdly, two reanalysis data sets were used to investigate the impact of the atmospheric boundary conditions. Finally, the model was run with three different horizontal grid spacings to investigate its effect on the flow near the coast.

An evaluation of the wind profile using vertical profilers revealed a small impact of using different set-ups on the estimated mean wind speed. The largest differences were due to using different PBL schemes. Both schemes slightly under predicted the wind speed at heights above 200 m. Larger differences between the different simulations were observed when comparing the RMSE between modelled and measured wind, with the set-ups using ERA interim data and the MYJ scheme having lower RMSEs than the set-ups using FNL data and the YSU scheme, respectively. The simulations with 1 and 0.5 km horizontal grid spacing in the inner domain had a larger RMSE than those with a 2 km spacing. This effect is well known in the verification of meteorological weather forecasts (Mass et al., 2002) because the RMSE is penalized by even small timing and spatial errors. The timing errors might be irrelevant when one is interested in overall wind climate of a particular region.

Horizontal transects of mean wind speed across the coastline measured with the scanning lidars were compared with the model simulations. The shape of the horizontal gradient agreed well with the measurements, but generally the modelled mean wind speed was slightly higher than observed. Furthermore the mean wind speed from the scanning lidar was higher than that observed using the vertically profiling lidars. The maximum difference in mean wind speed between different model set-ups was not more than $\approx 0.7 \text{ m s}^{-1}$. When measurements up to 2 km from the coastline were selected, the data availability was increased and the difference in mean wind speed between different simulations became even smaller. At 50 m asl the wind speed decreased more than predicted by the model simulations when moving from west to east across the coastline.

All model set-ups were evaluated using all available vertically profiling lidars and the meteorological mast at all heights. The results were analysed using Taylor diagrams and it was shown that using the MYJ instead of the YSU scheme and using the ERA interim instead of the FNL data reduced the RMSE and increased the correlation coefficient between model output and the observations, but also caused a slightly lower variance compared to the observations. The influence of using CORINE instead of USGS land cover data was only noticeable between 10–50 m above the surface, where the simulations using the CORINE data had a lower RMSE and higher correlation coefficient between modelled and measured winds. Using the two different SST descriptions as input did not have a large impact on the computed error metrics. The set-ups with horizontal grid spacing of 1 and 0.5 km had a higher RMSE and lower correlation coefficient, suggesting that a higher resolution is not needed to better resolve the coastal flow in the RUNE area.

When comparing the wind climatology produced by the various WRF model configurations, very small sensitivity is found. When examining the RUNE region, at 100 m all simulations (e.g. different configurations and model physics) are in excellent agreement in the mean wind speed right off the coast and differences increase both further offshore and inland. In general, offshore the WRF model using the YSU scheme is more sensitive to variations in landuse near the coastline and SST and forcing than simulations using the MYJ scheme. The forcing data has an impact on the simulated wind resources offshore, but the impact is negligible in the immediate RUNE region. The variance of the YSU-based model winds is larger than that of the MYJ-based ones, but varies little as a function of the model grid spacing. This has implications when

calculating power density and AEP from WRF model output.

Despite the short measuring period of RUNE and the absence of an accurate estimation of the wind speed at 5 km offshore for the whole four month period, a wind resource assessment was performed using the scanning lidar and the WRF model with the WAsP software as a reference. The mean wind speed 5 km offshore predicted by the WRF model was $\approx 13.8 \text{ m s}^{-1}$, whereas the estimations of the WAsP model ranged from $13.7\text{--}14.2 \text{ m s}^{-1}$. During the short period in which measurements were available at 5 km offshore, the mean wind speed from the model simulations differed with less than 3.3% from those obtained from the dual and sector-scan setup. The mean wind speed estimation of the scanning lidars for the whole period was dependent on the filtering, which is an issue that should be addressed before using scanning lidars for near-shore wind resource estimations.

References

- Anderson, J. R., Harde, E. E., Roach, J. T., and Witmer, R. E. (1976). *A land use and land cover classification system for use with remote sensor data*. US Government Printing Office, Washington, USA, vol. 964 edition.
- Badger, J., Volker, P. J. H., Hahmann, A. N., Hansen, J. C., and Hansen, B. O. (2015). Wind resource mapping in Vietnam : mesoscale modelling report. Technical report, World Bank Group, Energy Sector Management Assistance Program (ESMAP), Washington DC, USA.
- Barthelmie, R. J. (1999). The effects of atmospheric stability on coastal wind climates. *Meteorol. Appl.*, 6(1):39–47.
- De Meij, A. and Vinuesa, J. (2014). Impact of SRTM and Corine Land Cover data on meteorological parameters using WRF. *Atmos. Res.*, 143:351–370.
- Dee, D. P., Uppala, S. M., Simmons, A. J., Berrisford, P., Poli, P., Kobayashi, S., Andrae, U., Balmaseda, M. a., Balsamo, G., Bauer, P., Bechtold, P., Beljaars, a. C. M., van de Berg, L., Bidlot, J., Bormann, N., Delsol, C., Dragani, R., Fuentes, M., Geer, a. J., Haimberger, L., Healy, S. B., Hersbach, H., Hólm, E. V., Isaksen, L., Kållberg, P., Köhler, M., Matricardi, M., McNally, a. P., Monge-Sanz, B. M., Morcrette, J.-J., Park, B.-K., Peubey, C., de Rosnay, P., Tavolato, C., Thépaut, J.-N., and Vitart, F. (2011). The ERA-Interim reanalysis: configuration and performance of the data assimilation system. *Q. J. R. Meteorol. Soc.*, 137(656):553–597.
- Floors, R., Gryning, S.-E., Peña, A., and Batchvarova, E. (2011). Analysis of diabatic flow modification in the internal boundary layer. *Meteorol. Zeitschrift*, 20(6):649–659.
- Floors, R., Lea, G., Peña, A., Karagali, I., and Ahsbahs, T. (2016a). Report on RUNE’s coastal experiment and first inter-comparisons between measurements systems. Technical Report E-0115, DTU Wind Energy, Roskilde, Denmark.
- Floors, R., Lea, G., Peña, A., Vasiljević, N., Simon, E., and Courtney, M. (2016b). The RUNE Experiment—A Database of Remote-Sensing Observations of Near-Shore Winds. *Remote Sens.*, (in press).
- Floors, R., Vincent, C. L., Gryning, S.-E., Peña, A., and Batchvarova, E. (2013). The Wind Profile in the Coastal Boundary Layer: Wind Lidar Measurements and Numerical Modelling. *Boundary-Layer Meteorol.*, 147(3):469–491.
- Gemmill, W. and Katz, B. and Li, X. (2007). Daily real-time global sea surface temperature—High resolution analysis at NOAA/NCEP. Technical report, NCEP/NOAA.
- Gryning, S.-E., Floors, R., Peña, A., Batchvarova, E., and Brümmner, B. (2016). Weibull Wind-Speed Distribution Parameters Derived from a Combination of Wind-Lidar and Tall-Mast Measurements Over Land, Coastal and Marine Sites. *Boundary-Layer Meteorol.*, 159(2):329–348.
- Guo, Z., Xiao, X., Guo, Z., and Xiao, X. (2014). Wind Power Assessment Based on a WRF Wind Simulation with Developed Power Curve Modeling Methods. *Abstr. Appl. Anal.*, 2014:1–15.
- Hahmann, A. N., Vincent, C. L., Peña, A., Lange, J., and Hasager, C. B. (2015). Wind climate estimation using WRF model output: method and model sensitivities over the sea. *Int. J. Climatol.*, 35(12):3422–3439.
- Høyer, J. L. and Karagali, I. (2016). Sea Surface Temperature Climate Data Record for the North Sea and Baltic Sea. *J. Clim.*, 29(7):2529–2541.
- Høyer, J. L. and She, J. (2007). Optimal interpolation of sea surface temperature for the North Sea and Baltic Sea. *J. Mar. Syst.*, 65(1-4):176–189.
- Janjić, Z. I. (1990). The Step-Mountain Coordinate: Physical Package. *Mon. Weather Rev.*, 118(7):1429–1443.

- Lange, B., Larsen, S., Højstrup, J., and Barthelmie, R. (2004). Importance of thermal effects and sea surface roughness for offshore wind resource assessment. *J. Wind Eng. Ind. Aerodyn.*, 92(11):959–988.
- Mass, C. F., Ovens, D., Westrick, K., and Colle, B. A. (2002). Does increasing horizontal resolution produce more skillful forecasts? *Bull. Am. Meteorol. Soc.*, 83(March):407–430.
- Nielsen, J. R. (2013). *Representing vegetation processes in hydro-meteorological simulations using the WRF model*. Phd thesis, Risø-PhD-0016(EN), Risø National Laboratory for Sustainable Energy, Technical University of Denmark, Roskilde, Denmark, 128 pp.
- Noh, Y., Cheon, W. G., and Hong, S. Y. (2003). Improvement of the K-profile Model for the Planetary Boundary Layer based on Large Eddy Simulation Data. *Boundary-Layer Meteorol.*, 107(2):401–427.
- Nunalee, C. G. and Basu, S. (2014). Mesoscale modeling of coastal low-level jets: implications for offshore wind resource estimation. *Wind Energy*, 17(8):1199–1216.
- Pindea, N., Jorba, O., Jorge, J., and Baldasano (2002). Using NOAA-AVHRR and SPOT-VGT data to estimate surface parameters : application to a mesoscale meteorological model. *1st Int. Symp. Recent Adv. Quant. Remote Sens.*, 1161(June):16–20.
- Saha, S., Moorthi, S., Pan, H.-L., Wu, X., Wang, J., Nadiga, S., Tripp, P., Kistler, R., Woollen, J., Behringer, D., Liu, H., Stokes, D., Grumbine, R., Gayno, G., Wang, J., Hou, Y.-T., Chuang, H.-Y., Juang, H.-M. H., Sela, J., Iredell, M., Treadon, R., Kleist, D., Van Delst, P., Keyser, D., Derber, J., Ek, M., Meng, J., Wei, H., Yang, R., Lord, S., Van Den Dool, H., Kumar, A., Wang, W., Long, C., Chelliah, M., Xue, Y., Huang, B., Schemm, J.-K., Ebisuzaki, W., Lin, R., Xie, P., Chen, M., Zhou, S., Higgins, W., Zou, C.-Z., Liu, Q., Chen, Y., Han, Y., Cucurull, L., Reynolds, R. W., Rutledge, G., and Goldberg, M. (2010). The NCEP Climate Forecast System Reanalysis. *Bull. Am. Meteorol. Soc.*, 91(8):1015–1057.
- Sanz Rodrigo, J., Chávez Arroyo, R. A., Moriarty, P., Churchfield, M., Kosović, B., Réthoré, P.-E., Hansen, K. S., Hahmann, A., Mirocha, J. D., and Rife, D. (2016). Mesoscale to microscale wind farm flow modeling and evaluation. *Wiley Interdiscip. Rev. Energy Environ.*
- Skamarock, W. C., Klemp, J. B., Dudhia, J., Gill, D. O., Barker, D. M., Duda, M. G., Huang, X.-Y., Wang, W., and Powers, J. G. (2008). A description of the Advanced Research WRF version 3. Technical report, NCAR/TN-475+ STR, 113 pp. Mesoscale and Microscale Meteorology Division, National Center for Atmospheric Research, Boulder.
- Taylor, K. E. (2001). Summarizing multiple aspects of model performance in a single diagram. *J. Geophys. Res. Atmos.*, 106(D7):7183–7192.
- Troen, I. and Petersen, E. L. (1989). *European Wind Atlas*. Risø National Laboratory, Roskilde, Denmark.
- Vincent, C. L., Hahmann, A. N., Vincent, C. L., and Hahmann, A. N. (2015). The Impact of Grid and Spectral Nudging on the Variance of the Near-Surface Wind Speed. *J. Appl. Meteorol. Climatol.*, 54(5):1021–1038.
- Wyngaard, J. C. (2004). Toward Numerical Modeling in the “Terra Incognita”. *J. Atmos. Sci.*, 61(14):1816–1826.

A CORINE roughness classification

ID	CLC-code	Description	Roughness length [m]
1	111	Continuous urban fabric	1
2	112	Discontinuous urban fabric	0.5
3	121	Industrial or commercial units	0.5
4	122	Road and rail networks and associated land	0.075
5	123	Port areas	0.5
6	124	Airports	0.005
7	131	Mineral extraction sites	0.005
8	132	Dump sites	0.005
9	133	Construction sites	0.5
10	141	Green urban areas	1.1
11	142	Sport and leisure facilities	0.5
12	211	Non-irrigated arable land	0.05
13	212	Permanently irrigated land	0.05
14	213	Rice fields	0.05
15	221	Vineyards	0.1
16	222	Fruit trees and berry plantations	0.1
17	223	Olive groves	0.1
18	231	Pastures	0.03
19	241	Annual crops associated with permanent crops	0.1
20	242	Complex cultivation patterns	0.3
21	243	Land principally occupied by agriculture	0.3
22	244	Agro-forestry areas	0.3
23	311	Broad-leaved forest	0.8
24	312	Coniferous forest	0.8
25	313	Mixed forest	0.8
26	321	Natural grasslands	0.03
27	322	Moors and heathland	0.03
28	323	Sclerophyllous vegetation	0.03
29	324	Transitional woodland-shrub	1.1
30	331	Beaches, dunes, sands	3e-04
31	332	Bare rocks	0.005
32	333	Sparsely vegetated areas	0.005
33	334	Burnt areas	1.1
34	335	Glaciers and perpetual snow	0.001
35	411	Inland marshes	0.05
36	412	Peat bogs	5e-04
37	421	Salt marshes	0.05
38	422	Salines	5e-04
39	423	Intertidal flats	5e-04
40	511	Water courses	2e-04
41	512	Water bodies	2e-04
42	521	Coastal lagoons	2e-04
43	522	Estuaries	2e-04
44	523	Sea and ocean	2e-04

Table 7. Classification of the roughness length to the land cover classes of the CORINE data when used in the WAsP model.

DTU Wind Energy
Technical University of Denmark

Frederiksborgvej 399
4000 Roskilde
Denmark
Phone +45 4677 5024

www.vindenergi.dtu.dk